VRIJE
UNIVERSITEIT
BRUSSEL

Thesis submitted in order to obtain the degree of master in Physics and Astronomy

A NEW WINDOW FOR LEPTOPHILIC DARK MATTER

Sam Junius

June 19, 2018

Promotors:
Prof. Dr. Alberto Mariotti and Prof. Dr. Laura Lopez Honorez
Sciences & Bio-Engineering Sciences

Abstract

Until now, no evidence has been found for dark matter in particle physics experiments. The lack of any dark matter signal has put a lot of pressure on the most popular paradigms for dark matter such as the Weakly Integrating Massive Particle. Therefore, it is time to consider other dark matter candidates beyond the WIMP. We consider a simplified model where the standard model is extended with one Majorana fermion and a charged scalar coupling to the standard model leptons through a Yukawa interaction, hence a ”leptophilic dark matter model”. We investigate a new mechanism for dark matter production in the early universe that differs from the standard freeze-out which is relevant for the WIMP scenario. This alternative mechanism is called conversion-driven freeze-out and will reproduce the correct relic dark matter abundance if the mass-splitting between the dark matter and charged scalar and the coupling constant are sufficiently small. This regime opens a new window on dark matter phenomenology. In particular, the small coupling constant leads to a macroscopic decay length of the charged scalars giving rise to exotic signals at collider experiments like disappearing charged track or displaced leptons plus missing energy.

Foreword

During the final year of my master studies, I spend most of my time working on my thesis. It would be the highlight of the five years I have been studying at the VUB. I think I can say I delivered a good thesis of which I am proud of. However, I would have not been able to do this without the help of some people who followed my progress closely. First of all, I want to thank my promotors Alberto Mariotti and Laura Lopez Honorez. We met every week such that I could report what I did during the week. In this way, they were always up to date with my progress and I could always ask questions whenever I needed. This helped me a lot. From the moment I got stuck, I could go to one of them and together, we managed to solve the problems that blocked my path. Besides that, they also helped me by improving my skills to write and present this thesis. Without them, I would not have achieved all of this, so I am really grateful to have them as my promotors.

Besides my promotors, Matthias Vereecken was also a great support during the year. Mainly because in the first semester, he helped me a lot starting up the project. In order to do the research, I worked with some software packages I had never worked with before. Matthias always provided me with information and answers to my questions to get to know these software packages. He also followed my work closely and was always prepared to give me some very helpful tips in orders to write my thesis. Therefore, I also want to thank Matthias for his help throughout the whole year.

Contents

Introduction

The existence of Dark Matter (DM) in the universe has been established by a number of astrophysical observations based on gravitational interactions. It is also included in the standard model of cosmology to account for observations that can not be explained without the presence of dark matter. For instance, DM is able to explain the observed anisotropies of the CMB. From these observations, scientists established that dark matter constitutes nearly 85% of the total matter content in the universe we observe today. A large amount of models describing DM as a fundamental particle have already been proposed, but none of these are confirmed by experiments yet. Because we have been able to deduce the amount of DM in the universe, it is very important to study how these fundamental DM particles can be produced in the early universe. A number of production mechanisms are already explored. In the WIMP paradigm, the DM shares sizeable interactions with the visible sector such that the relic abundance is set by the freeze-out mechanism [1]. Alternatively, it could be that dark matter couples more weakly to the SM particles and to itself such as in the case of so-called superWIMPs [2] and FIMPs [3]. These hypothetical particles are produced via other mechanisms. Other possibilities are that dark matter is very weakly coupled to the visible sector, but has substantial couplings with a hidden sector to which it is equilibrated [4] or that there is an asymmetry in the number densities of the DM and its anti-particle [5].

Despite many attempts to observe a clear DM signal, nothing has been seen yet. The no-observation of dark matter is starting to put some pressure on popular models like the WIMP paradigm. Because these models are now under such constraints by experimental results, other models are more and more considered. In general, dark matter candidates should appear in the context of an extension of the Standard Model (SM) that is UV complete. Alternatively, a more bottom up approach of simplified models is often considered. These models can capture the relevant phenomenological features without the complication of a complete UV model. They are constructed by adding just a few particles to the standard model and require some simple assumptions in order to be consistent (gauge invariance, renormalizable, etc).

Simplified models may not be the complete description of nature, we can still learn a lot from them. For instance, we can study how DM interacts with the SM particles. This is very important for detection experiments. Due to the absence of a clear DM signal, physicists are starting to look for more exotic signatures, like displaced vertices plus missing energy at collider experiments. They occur when the dark matter couples very weakly to the standard model particles. Simplified models can be used to explain how these exotic signatures can arise. When such a signature would be observed, simplified models can help interpreting the data to gain knowledge about the properties of the DM.

In chapter 1 of this thesis, we start by introducing the concept of dark matter. A review of the most convincing evidence and most popular dark matter candidates are given. Some of the evidence implies that dark matter must be present already in the early universe, right after the big bang. Therefore, we also review some possible ways dark matter can be produced in the early universe. To conclude this chapter, we discuss the main strategies how dark matter can be detected.

As we already mentioned, simplified models are useful to describe DM and characterize their phenomenology at colliders as well in detection experiments. In chapter 2 we introduce the simplified model that we will further consider in this thesis. It consists in adding a Majorana DM candidate to the standard model together with a co-annihilating scalar particle which is charged under the standard model gauge groups. The dark matter particle is coupled to the SM particles through a Yukawa interaction involving the charged scalar particles and SM leptons. Hence, we name the DM candidates in this simplified model as leptophilic dark matter. The strength of the interactions is controlled by a coupling constant λ_χ. Depending on the value of this coupling, the way the dark matter is produced in the early universe changes. We give an overview of all the different mechanisms and in which regimes they are important. Moreover, we go beyond the standard mechanisms that we introduced in chapter 1 to explore a new window for leptophilic DM. In particular, an alternative mechanism called conversion-driven freeze-out is introduced. At the end of this chapter, the dependence on the initial conditions of the production mechanisms is studied.

The conversion-driven freeze-out mechanism we introduced in chapter 2 is studied in more detail in chapter 3 in the context of the leptophilic dark matter simplified model. We explain why we introduced it and in which region of parameter space it is relevant. After this, we investigate the lifetime of the charged scalar in this region of parameter space. This will be done to study when the model exhibits exotic collider signatures at for instance the LHC.

In chapter 4, we discuss how exotic signatures such as displaced vertices can be observed at collider searches. We first give an overview of the purpose of the most important parts of a detector to then see how exotic signals can occur in these detectors. The most important searches for such signatures are reviewed before they are applied to the simplified model from chapter 2 in order to display the reach of the LHC on conversion-driven freeze-out for leptophilic DM.

Chapter 1

Dark Matter

1.1 Short history of dark matter

Since the publication of Newton's *"Philosophiae Naturalis Principia Mathematica"* in 1687, science made a great leap forward in explaining the motion of astrophysical objects. Not only did his gravitation law teach us a lot, also deviation from it deepened our understanding of the Universe. Whenever anomalies were observed, one question came to mind. Is this anomaly an indication that the laws of gravitation are incorrect or a hint of something new and unseen. For instance, the observed anomaly of the motion of Uranus led to the prediction of a new planet, Neptune, which was later visually discovered in 1846. In this case, the second option proved to be the correct one. One has to be careful by just assuming one of the two options because later, the existence of a planet called Vulcan was predicted to explain the anomalous motion of Mercury. This planet was never found, simply because it does not exist. The problem of the anomalous motion of Mercury was later resolved by Einstein's theory of general relativity, which is more precise than Newton's law of gravitation.

In 1933, a very similar problem occurred. The Swiss-American astronomer Fritz Zwicky studied the redshift of various galaxy clusters [7] that were published by Edwin Hubble and Milton Humason in 1931 [8]. He was particularly interested in the Coma Cluster, where he noticed differences in the apparent velocity of some galaxies that exceed 2000 km/s. This fact triggered him to do a further analysis by applying the virial theorem in order to estimate the mass of this cluster. Starting from a velocity dispersion of 700 km/s, he found a conservative lower limit of $M_{cluster} > 4.5 \times 10^{13} M_{\odot}$. When assuming an average luminosity of $L = 8.5 \times 10^{7} L_{\odot}$ for the cluster galaxies, his results implied a very high mass-to-light ratio of about 500. This meant that there was some amount of mass that we were not able to observe, which from then on is referred to as Dark Matter (DM).

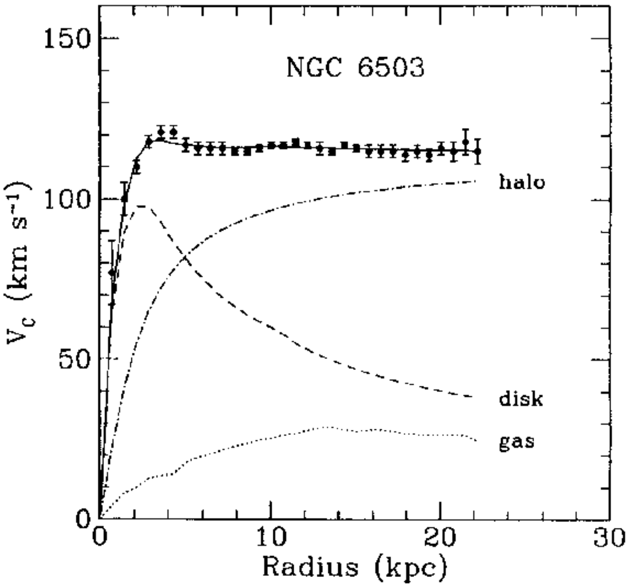

Figure 1.1: Galactic rotation curve for NGC 6503 showing disk and gas contribution plus the dark matter halo contribution needed to match the data [10].

A second anomaly that was noticed some years later has to do with rotation curves of galaxy clusters. In 1939, Horace Babcock presented the rotation curve of M31 out to about 20 kpc away from its centre [9]. He found very high and quasi constant values of the circular velocity at large radii. Later, the same behaviour was found in many other galaxies, like NGC 6503 (see figure 1.1). This result was quite surprising because one would expect that the circular velocity would go down if we look at larger radii, $v_c \propto 1/\sqrt{R}$. Babcock calculated that this flat rotation curve implies that there must be large amounts of mass in the outer parts of the galaxy. With this second anomaly, the lack of observable mass was a problem that could not be ignored any more.

Again, the same question did arise. Is this dark matter something real/physical that we just have not observed yet, or might it be that this anomaly is just due to the fact that we are applying a theory that is not valid on the large scales we are applying it. This question split researchers into two groups. One group was eager to find again a new correction of Newton's law of gravitation to explain this flat rotation curves. They came up with a new theory called MOND [11] (MOdified Newtonian Dynamics). However, later evidence showed that the option of Dark Matter being something physical is the more probably answer to the question.

1.1.1 More evidence for dark matter

CMB

Another clue for the dark matter comes from the Cosmic Background Radiation (CMB). This background radiation originates from the propagating photons in the early Universe, once they decoupled from matter. It is observed that the CMB is isotropic up to the 10^{-5} level and behaves like a black body with temperature $T = 2.726K$ with an extraordinary precision. However, when COBE [12] (COsmic Background Explorer) and later WMAP [13] (Wilkinson Microwave Anisotropy Probe) started to take data, it became clear that there are small anisotropies ($\frac{\delta T}{T} < 10^{-5}$). This can help to probe the seeds for matter density perturbations at the origin of the large scale structure that we see in the sky today. From the study of the CMB spectrum, comparing with what would result from a theoretical cosmology model, it appears that there must have been some extra form of matter, apart from baryonic matter, in the Universe at the time of decoupling such that structure formation could start. From the WMAP data alone, cosmologist were even able to extract the abundance of baryonic matter ($\Omega_b h^2$) and the total amount of matter ($\Omega_m h^2$) in the Universe [14],

$$\begin{aligned} \Omega_b h^2 &= 0.0224 \pm 0.0009, \\ \Omega_m h^2 &= 0.135^{+0.008}_{-0.009}. \end{aligned} \tag{1.1}$$

In 2009, a new experiment was launched to take more data of the CMB. The Planck Satellite was even able to determine a precise value for the relic DM abundance [15]

$$\Omega_{DM} h^2 = 0.1198 \pm 0.0015. \tag{1.2}$$

Gravitational lensing

One of the consequences of the general theory of relativity (GR) described by Einstein is that light rays do not always follow a straight trajectory but are bent around gravitating masses. Thus, just like optical lenses, celestial bodies can serve as gravitational lenses to refract light although the physics behind the two processes is completely different. The amount of bending depends on the mass of the bodies, whether it is baryonic or otherwise. Gravitational lensing can be a very important tool in the search to dark matter. There are three types of lensing (microlensing, weak and strong lensing [16]) and each of them can teach us new things about the masses and mass distribution of celestial bodies. For instance, it has been observed that individual galaxies are surrounded by a halo of dark matter. Gravitational lensing can be used to probe the properties and distribution of this halo, even to very large radii beyond the scope of other tracers of mass [17].

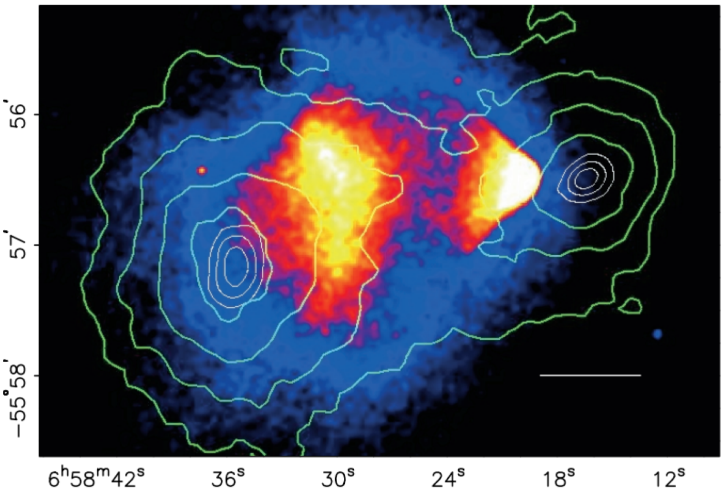

Figure 1.2: An X-ray image of the bullet cluster, obtained with a 500 second exposure with Chandra. The colors denote the X-ray temperature of the gas where blue indicates the coolest. The white bar represents a distance of 200kpc and the green contours denote the reconstructed lensing signal, proportional to the projected mass in the system [18].

The bullet cluster

One of the most recent observations that has been seen as a direct empirical proof of the existence of dark matter is the bullet cluster. This cluster is actually made out of two clusters that crossed each other recently. The distribution of stars and galaxies can be resolved from the hot X-ray emitting gas (which constitutes the majority of the baryonic mass in the system). One can compare this X-ray map with results from weak lensing where the total mass distribution is tracked. As can be seen in figure 1.2, the comparison clearly reveals that most of the mass does not trace the distribution of the baryonic mass in the system. This again reveals that something else than usual matter must dominate the mass of the cluster. Many researchers saw this observation as the ultimate argument to prefer dark matter over theories such as MOND because this measurement does not depend on dynamical assumptions, something MOND tries to adapt to explain other observations.

1.2 Dark matter candidates

As we briefly discussed in the previous section, there is a compelling amount of evidence for the existence of dark matter. The natural question to ask next is ”what is dark matter made of?”. This is a question that has been keeping scientists busy for several decades. Firstly, scientists started to look at what they knew that existed, like for instance the particles in the Standard Model (SM). Most of these particles could be almost immediately discarded (most of them are charged) until only one remained, the neutrinos. They were considered as an excellent DM candidate because they are neutral and only interact weakly with the other SM particles. However, one can predict the relic density abundance [14]

$$\Omega_\nu h^2 = \sum_{i=1}^{3} \frac{m_i}{93eV}, \tag{1.3}$$

where i is the generation of the neutrino. The mass of neutrinos are not known exactly yet, but constraints are already available and come from experiments such as the tritium β-decay at Troitsk and Mainz [19]. If we use the upper limits, we also find an upper bound for the abundance

$$\Omega_\nu h^2 < 0.07, \tag{1.4}$$

which is much smaller than the observed value of 0.12. This means that neutrinos are not abundant enough to be the dominant DM component. Also other arguments discarded SM neutrinos as a viable DM candidate [14] and therefore, there is no known particle left that could be the DM. Since then, a lot of new models for dark matter have been proposed, but until now, there is no experimental evidence for one of these. Here, we shortly review some of the most discussed candidates.

1.2.1 Undiscovered fundamental particles

The standard model of particle physics is known to be incomplete, and this is not only due to the lack of a DM candidate. Even from a theoretical point of view, there are some severe problems. The hierarchy problem [20] is one of them. The problem here is that the Higgs mass m_H receives large quantum corrections from the virtual effects of every particle that couples to the Higgs field. In order to solve this and other problems, scientists started to predict extensions of the standard model that could potentially resolve these problems. A lot of these models predict new particles of which some of them are viable DM candidates. Here, we give a short list of the most important ones:

- Sterile Neutrinos, a neutrino like particle that does not interact via the weak force [21],
- Kaluza-Klein states appear in models with extra dimension [22],
- Axions are a solution for the strong CP problem of the standard model [23, 24].

Another important model is called supersymmetry (SUSY) and gives a possible solution for the hierarchy problem. In the SM, there are two types of particles called fermions, particles with half-integer spin, and bosons with integer spin. Supersymmetry states that there is a new kind of symmetry such that every boson has a fermionic partner with the same quantum numbers and vice versa [25]. This symmetry solves the hierarchy problem because the quantum corrections of fermions and scalars with the same quantum numbers cancel each other exactly. If SUSY is a symmetry of nature, at least the superpartners of the SM particles should exist. The supersymmetric model that contains the minimal amount of particles and also includes the standard model is called the Minimal Supersymmetric Standard Model (MSSM). The MSSM predicts not only a superpartner for each SM particle, but also a second Higgs doublet. Otherwise, the theory would be inconsistent [25]. The particle content of the MSSM is summarized in table 1.1. There are a lot of new particles in this model and therefore, a lot of DM candidates. The most important ones for DM purpose are the neutralinos, a mixture of the four neutral superpartners of the Higgs, SU(2) and U(1) gauge bosons. To make the lightest one stable, we need a $\mathbb{Z}_2$ symmetry under which all SM particles are even and their superpartners are odd. Therefore, all superparticles can only decay to at least one other superparticle. It is kinematically forbidden that the lightest superparticle decays to other superparticles causing it to be stable. In SUSY, such a $\mathbb{Z}_2$ symmetry is assumed and is called R-parity [25]. Therefore, the lightest superparticle is a possible DM candidate.

If supersymmetry is a real symmetry, all the particles of the MSSM must exist. Nevertheless, this does not mean that we are restricted to those particles in the search for dark matter. For instance, one of the main defects of the standard model is that only three of the four fundamental forces are present. Therefore, physicists have already postulated the existence of the graviton, a hypothetical spin-2 boson that mediates gravity. If this particle really exists and SUSY is a correct symmetry of nature, also its superpartner called the gravitino should exist. This is a stable, neutral particle and is therefore often stated as a good DM candidate. Together with the neutralino, the gravitino is currently the most studied supersymmetric DM candidates.

1.2.2 Primordial Black Holes

When the dark matter problem was stated for the first time, the first candidates to explain the problems were mostly compact astrophysical objects, such as black holes. Very quickly, it was found that most of these objects are not suitable as dark matter, except for Primordial Black Holes (PBH) [26]. PBHs are black holes that are already formed very early in the history of the universe when the density was very high, well before stars and therefore stellar black holes, which originate

Names		spin 0	spin 1/2	$SU(3)_C,\ SU(2)_L,\ U(1)_Y$
squarks, quarks	Q	$(\widetilde{u}_L\ \ \widetilde{d}_L)$	$(u_L\ \ d_L)$	$(\ \mathbf{3},\ \mathbf{2}\ ,\ \frac{1}{6})$
(×3 families)	$\overline{u}$	$\widetilde{u}^*_R$	$u^\dagger_R$	$(\ \overline{\mathbf{3}},\ \mathbf{1},\ -\frac{2}{3})$
	$\overline{d}$	$\widetilde{d}^*_R$	$d^\dagger_R$	$(\ \overline{\mathbf{3}},\ \mathbf{1},\ \frac{1}{3})$
sleptons, leptons	L	$(\widetilde{\nu}\ \widetilde{e}_L)$	$(\nu\ \ e_L)$	$(\ \mathbf{1},\ \mathbf{2}\ ,\ -\frac{1}{2})$
(×3 families)	$\overline{e}$	$\widetilde{e}^*_R$	$e^\dagger_R$	$(\ \mathbf{1},\ \mathbf{1},\ 1)$
Higgs, higgsinos	H_u	$(H^+_u\ \ H^0_u)$	$(\widetilde{H}^+_u\ \ \widetilde{H}^0_u)$	$(\ \mathbf{1},\ \mathbf{2}\ ,\ +\frac{1}{2})$
	H_d	$(H^0_d\ \ H^-_d)$	$(\widetilde{H}^0_d\ \ \widetilde{H}^-_d)$	$(\ \mathbf{1},\ \mathbf{2}\ ,\ -\frac{1}{2})$

(a) Chiral supermultiplets

Names	spin 1/2	spin 1	$SU(3)_C,\ SU(2)_L,\ U(1)_Y$
gluino, gluon	$\widetilde{g}$	g	$(\ \mathbf{8},\ \mathbf{1}\ ,\ 0)$
winos, W bosons	$\widetilde{W}^\pm\ \ \widetilde{W}^0$	$W^\pm\ \ W^0$	$(\ \mathbf{1},\ \mathbf{3}\ ,\ 0)$
bino, B boson	$\widetilde{B}^0$	B^0	$(\ \mathbf{1},\ \mathbf{1}\ ,\ 0)$

(b) Gauge supermultiplets

Table 1.1: Particle content of the MSSM [25]. The superpartners are denoted with a tilde.

from the collapse of a massive star, could form. Stellar BHs have already been observed, in contrast to PBHs, for which no compelling evidence existed. However, there is no clear evidence for any other DM candidate, so this is not something that should stop us from investigating PBHs. Unfortunately, there is one major problem for PBHs to be a good DM candidate. There are strong constraints on the masses from observations (for more information about these constraints, see [26]). There is only a small window of possibilities, which is shrinking throughout the years. Therefore, PBHs were less considered as a viable DM candidate. Interest regained when the LIGO collaboration detected gravitational waves coming from two merging black holes with a mass which is larger than typically expected from stellar black holes. This was seen as an indication for some new kind of BH, like PBHs [27]. The masses of the observed BHs fell also inside the small accessible region such that it could account for at least a part of the DM in the universe. Also the observed merging rates are compatible with the PBH models. Since then, research to PBH as a DM component has again been growing.

1.3 Dark matter production in the early universe

As already mentioned in section 1.1.1, we need dark matter in the early universe in order to start the formation of the large structures we observe in the sky. Therefore, it is necessary to study how the DM particles can be produced in the early universe. Here, we review the most studied production mechanisms.

1.3.1 Freeze-out

When the universe was only a few seconds old, it was really hot and dense. All the particles were very close together and because of that, their interactions occurred more frequently than they do today. For example, a photon in the universe today has a mean free path of about 10^{28} cm, while when the universe was only 1 second old, its mean free path was about the size of an atom. This means that all the particles in the universe were constantly scattering which kept them coupled to what cosmologists call the thermal bath, where they are in equilibrium. As long as the particles keep interacting fast enough with each other, they stay coupled to the thermal bath. However, the universe is expanding, so all the particles move away from each other and can not keep interacting fast enough, which means that at some point, they decouple from the thermal bath. This way of producing the dark matter is referred to as the freeze-out mechanism.

The freeze-out mechanism is used to predict the relic abundance of certain DM particles like the WIMP. The WIMP or Weakly Interacting, Massive Particle is a generic dark matter candidate that only interacts via the weak force (or another force with approximately the same strength) with the SM particles and has typically a mass of the order of the weak scale. In the freeze-out mechanism, the WIMP is initially in chemical equilibrium with the SM particles. In order to be in equilibrium, it must interact with the bath particles, for instance via the annihilation reaction $\chi\chi \leftrightarrow B_1 B_2$ where χ is the DM and B_1, B_2 are thermal bath particles. In general, any $\chi \leftrightarrow B$ reaction can keep the DM in equilibrium [28] but here, we assume for simplicity that the annihilation of χ drives the freeze-out. The analysis for another type of process is very similar. The cross section of the reaction must be large enough, otherwise equilibrium can not be maintained. To find the final DM abundance, we have to solve the Boltzmann equation for this reaction, which governs the evolution of the abundances n_i of all the particles participating in the reaction. We are typically interested in systems at temperatures smaller than $E - \mu$ where E is the energy of the initial particles and μ is the chemical potential. In this limit, we can neglect Bose-Einstein and Fermi-Dirac statistics and just assume a general Maxwell-Boltzmann distribution. For a general reaction $1 + 2 \to 3 + 4$ with thermally averaged cross section $\langle\sigma v\rangle$, the Boltzmann equation is given by [29]

$$a^{-3}\frac{d(n_1 a^3)}{dt} = \langle\sigma v\rangle n_{1,eq} n_{2,eq}\left(\frac{n_3 n_4}{n_{3,eq} n_{4,eq}} - \frac{n_1 n_2}{n_{1,eq} n_{2,eq}}\right), \tag{1.5}$$

where

$$n_{i,eq} = g_i \int \frac{d^3 p_i}{(2\pi)^3} f_i(E_i). \tag{1.6}$$

$f_i(E)$ is the phase space distribution and g_i is the number of degrees of freedom of the i^{th} particle in the reaction. As already mentioned, we can approximate $f_i(E)$ by the Boltzmann distribution,

$$n_{i,eq} = g_i \int \frac{d^3 p_i}{(2\pi)^3} e^{-E_i/T} = \left\{ \begin{array}{ll} g_i \left(\frac{m_i T}{2\pi}\right)^{3/2} e^{-m_i/T} & \text{for } m_i \gg T \\ g_i \frac{T^3}{\pi^2} & \text{for } m_i \ll T \end{array} \right. . \tag{1.7}$$

The thermally averaged cross section $\langle\sigma v\rangle$ can be obtained by [29]

$$\langle\sigma v\rangle = \frac{1}{n_{1,eq} n_{2,eq}} \prod_{i=1}^{4} \int \frac{d^3 p_i}{(2\pi)^2 2E_i} (2\pi)^4 \delta^3(p_1 + p_2 - p_3 - p_4) \\ \delta(E_1 + E_2 - E_3 - E_4)|\mathcal{M}|^2, \tag{1.8}$$

where E_i and p_i are the energy and three-momentum of the particles involved in the reaction and $\mathcal{M}$ the Feynman amplitude. For the case of DM annihilation into bath particles which are in chemical equilibrium (i.e. $n_B = n_{B,eq}$), the Boltzmann equation becomes

$$a^{-3}\frac{d(na^3)}{dt} = \langle\sigma v\rangle [n_{\chi,eq}^2 - n_\chi^2], \tag{1.9}$$

where a is the cosmological scale factor. From equation (1.9) and the fact that

$$a^{-3}\frac{d(na^3)}{dt} = \frac{dn}{dt} + 3Hn, \tag{1.10}$$

where $H = \frac{\dot{a}}{a}$ is the Hubble constant, we can already predict how the DM abundance behaves through the evolution of the universe. To compare the cross section with the Hubble rate, we define $\Gamma = n\langle\sigma v\rangle$. If this rate is much larger than H, the right hand side of equation (1.9) is much larger than the left hand side, unless $n \approx n_{eq}$. This means that as long as $\Gamma > H$, the annihilation process is efficient and the dark matter is in chemical equilibrium with the bath particles. However, from the moment the process becomes inefficient ($\Gamma < H$), the DM leaves equilibrium because there must be a large factor to compensate for the large Hubble rate in the Boltzmann equation (1.9).

In order to confirm this behaviour, we need to solve the Boltzmann equation exactly. To do this, we can rewrite equation 1.9. The density depends on the scale factor ($n \propto a^{-3}$). We can define some new variable to get rid of this dependence,

$$Y \equiv \frac{n}{s} \quad \text{and} \quad x \equiv \frac{m}{T}, \tag{1.11}$$

where m is the DM mass and s the entropy,

$$s = g_{*,s}\frac{2\pi}{45}T^3 = s(m)x^{-3}. \tag{1.12}$$

With this knowledge, and the fact that $\frac{dT}{dt} \approx -HT$, we can rewrite the Boltzmann equation to

$$\frac{dY}{dx} = \frac{\langle\sigma v\rangle s}{Hx}\left[Y_{eq}^2 - Y^2\right]. \tag{1.13}$$

In the radiation era, the era where radiation dominates over all other forms of energy and also the era where freeze-out happens [29], the Hubble constant equals

$$H = \sqrt{\frac{8\pi G}{3}\rho_R} = \sqrt{g_{*,\rho}\frac{\pi^2}{90}}\frac{T^2}{M_{Pl}} = H(m)x^{-2}. \tag{1.14}$$

Using this and equation (1.12), we are able to rewrite the Boltzmann equation (1.13) as

$$\frac{dY}{dx} = \frac{\langle\sigma v\rangle s(m)}{H(m)x^2}\left[Y_{eq}^2 - Y^2\right]. \tag{1.15}$$

Now we can solve this equation if we know $\langle\sigma v\rangle$ as a function of x. In general, this can be done by specialized software, but since the WIMP is a non-relativistic particle, we can expand the thermally averaged cross section $\langle\sigma v\rangle = a + bv^2 + \ldots$.

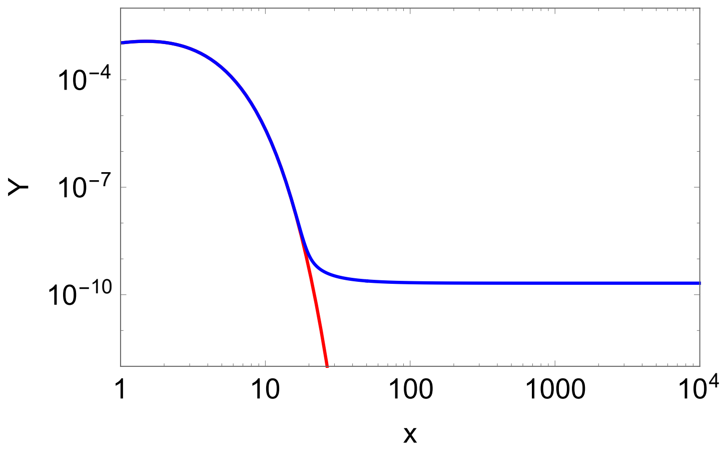

Figure 1.3: The numerical solution of the Boltzmann equation (blue) for a p-wave (p=2) and the equilibrium yield (red).

For a Boltzmann distribution, $\langle v \rangle \propto \sqrt{T}$ [30]. If the leading order term of the cross section goes like the p-th power of v in the expansion, we may write

$$\langle \sigma v \rangle = \langle \sigma v \rangle_0 x^{-p/2} = \langle \sigma v \rangle_0 x^{-n}. \tag{1.16}$$

Then, the Boltzmann equation becomes

$$\frac{dY}{dx} = \frac{\lambda}{x^{n+2}} \left[Y_{EQ}^2 - Y^2 \right], \tag{1.17}$$

where λ is a new constant defined as

$$\lambda = \frac{\langle \sigma v \rangle_0 s(m)}{H(m)}. \tag{1.18}$$

The Boltzmann equation in this form be solved numerically in a numerical software package like Mathematica [31]. This we do with our own code for a WIMP with mass $m = 1$ TeV. We take $\langle \sigma v \rangle_0 = 10^{-10}$ GeV^{-2}, which is a typical value for weak interactions, and $g_{*,\rho} = g_{*,s} = 100$. The result of this integration can be found in figure 1.3. We can see that the yield Y follows the equilibrium yield until it decouples at a certain time and freezes out. This happens when the annihilation of χ becomes inefficient due to the expansion of the universe, or in other words, when the annihilation rates becomes smaller than the Hubble rate. Thus, the higher the rate, the later the yield deviates from equilibrium and therefore, the lower the value of the final abundance of dark matter.

1.3.2 Freeze-in

Dark matter only experiences freeze-out if it is initially kept in equilibrium with the thermal bath particles. This is only possible if the coupling constant which drives this reaction is large enough. If it is too small to maintain equilibrium, we can not use the freeze-out mechanism to find the final abundance. Instead, we can have a Feebly Interacting Massive Particle (FIMP) which experiences the freeze-in mechanism. In this scenario, it is assumed that there is no other DM production mechanism such that the initial DM abundance is negligible. Then, the dominant contribution of the abundance comes from the production via inefficient reactions like the decay of a thermal bath particle into DM and another bath particle, $B_1 \to \chi B_2$, if $m_{B_1} > m_\chi + m_{B_2}$. Other reaction, like scattering, can also produce DM [32], but here we focus on the decay, which is the most studied case. The Boltzmann equation for this production mechanism reads [33]

$$\begin{aligned} a^{-3}\frac{d(na^3)}{dt} &= g_{B_1}\int \frac{d^3p_{B_1}}{(2\pi)^3 E_{B_1}} m_{B_1} f_{B_1} \Gamma_{B_1} \\ &= \frac{g_{B_1} m_{B_1} \Gamma_{B_1}}{2\pi^2}\int dE_{B_1}(E_{B_1}^2 - m_{B_1})^{1/2} e^{-E_{B_1}/T} \\ &= \frac{g_{B_1} m_{B_1}^2 \Gamma_{B_1}}{2\pi^2} T K_1(m_{B_1}/T), \end{aligned} \tag{1.19}$$

where $K_1(x)$ is the first modified Bessel function of the second kind, Γ_{B_1} the decay width of the decaying bath particle and g_{B_1} and m_{B_1} the number of degrees of freedom and mass of this particle. Just as before, we rewrite this in term of the yield Y and the variable $x = \frac{m_{B_1}}{T}$,

$$\frac{dY}{dx} = \frac{g_{B_1} m_{B_1}^3 \Gamma_{B_1}}{2\pi^2 s(m_{B_1}) H(m_{B_1})} x^3 K_1(x). \tag{1.20}$$

The final yield can be found by integrating this equation from the early universe until now. This means that we start from really high and go to quite low temperatures ($T_{today} = 2.7K$), so we might as well integrate form 0 to ∞. The integral of $x^3 K_1(x)$ gives a factor of $\frac{3\pi}{2}$, so we get

$$Y_\infty = \frac{3 g_{B_1} m_{B_1}^3 \Gamma_{B_1}}{4\pi s(m_{B_1}) H(m_{B_1})} = \frac{135 g_{B_1}}{8\pi^3 (1.66) g_{*,s}\sqrt{g_{*,\rho}}}\left(\frac{M_{Pl}\Gamma_{B_1}}{m_{B_1}^2}\right). \tag{1.21}$$

For the second equality, we used equations (1.12) and (1.14). Knowing this, we can calculate the final abundance,

$$\Omega h^2 = \frac{\rho}{\rho_{crit}} h^2 = \frac{m_\chi s_0 Y_\infty}{3(H_0/h)^2 M_{Pl}} = \frac{1.09 \times 10^{27} g_{B_1}}{g_{*,s}\sqrt{g_{*,\rho}}}\frac{m_\chi \Gamma_{B_1}}{m_{B_1}}. \tag{1.22}$$

If we want to see the evolution of the yield through time, we have to integrate equation (1.20) from zero to x for every value of x. This has been done with our

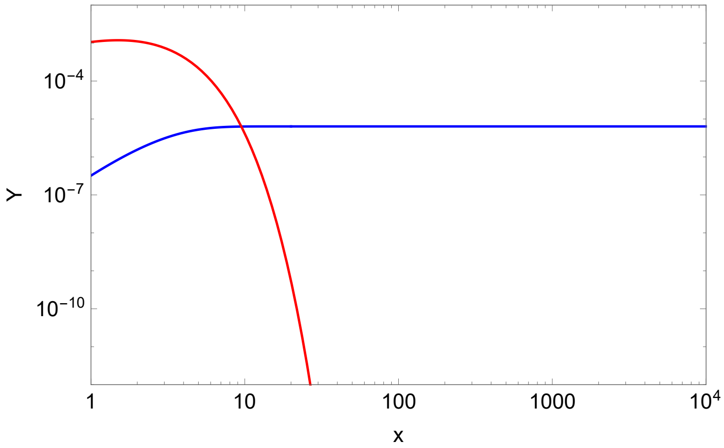

Figure 1.4: The DM yield (blue) obtained by numerical integrating equation (1.20) for a coupling constant of $y = 10^{-8}$ and the DM equilibrium yield (red) obtained from equation (1.7).

own code in figure 1.4 for χ being a scalar particle such that $\Gamma_{B_1} = \frac{m_{B_1} y^2}{8\pi}$ where $y = 10^{-8}$ is the coupling constant that drives the decay and $m_{B_1} = 1$ TeV. We see that we start out with a negligible yield that grows until it reaches the value we calculated in equation (1.21) and freezes in. In equation (1.21), we also see that the final abundance depends linearly on $\Gamma_{B_1} \propto y^2$ and thus for a larger coupling of the DM with the thermal bath particles, we obtain a larger final abundance. This is in contrast with the freeze-out mechanism, where a larger coupling meant a smaller final abundance. This behaviour is summarized in figure 1.5, where we see that for a small coupling, we have the freeze-in mechanism where the final abundance grows with the coupling constant and for larger values of y, we see the inverse behaviour of the freeze-out mechanism. For intermediate values, many scenarios exist which can be more complex as the behaviour we show in figure 1.5, see for instance [28].

1.3.3 Co-annihilations

Until now, we discussed the freeze-out and freeze-in mechanism for only one particle. Of course, it can be that there is more than one particle in the Dark Sector (DS) that couple to the DM. For the freeze-out mechanism, the situation can change due to the presence of other particles that are being produced through the same mechanism. The influence of other dark sector particles depends on the moment of decoupling of the DM and of the other particles. If they decouple at different times, we can separate the freeze-out processes for all different particles and the above methods can still be applied to calculate the relic abundance. The

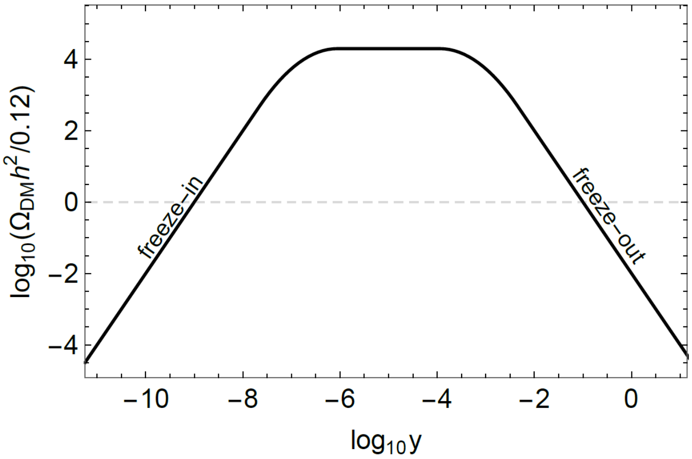

Figure 1.5: A schematic representation of the dependence of the final abundance on the coupling constant y of the DM with the thermal bath particles [34]. We see that for small values of y the abundance rises because we are in the freeze-in regime. For large values of y, the opposite happens because this is the freeze-out regime. For intermediate values of y, more complex scenarios can exist, see for instance [28].

moment of decoupling depends on the mass of the particle, so for two particles with a similar mass (compared to the temperature when freeze-out happens T_f), we need to take into account that they may decouple simultaneously if they have interactions of the same strength.

Let us consider that we have N dark sector particles χ_i that couple to the thermal bath with masses m_i and with degrees of freedom g_i. We take $m_i < m_j$ for $i < j$ such that χ_1 is the lightest one. Here, we also assume that there is some kind of $\mathbb{Z}_2$-symmetry under which all χ_i are odd and all the other (SM) particles are even. Due to this symmetry, all χ_i decay into at least one DS particle. Therefore, it is kinematically forbidden for the lightest DS particle χ_1 to decay, making it stable and thus a viable DM candidate.

The following reactions are able to change the abundances of the DS particles in the early universe,

$$\chi_i\chi_j \leftrightarrow B_1B_2, \tag{1.23}$$

$$\chi_iB_1 \leftrightarrow \chi_jB_2, \tag{1.24}$$

$$\chi_j \leftrightarrow \chi_iB_1B_2, \tag{1.25}$$

where B_1 and B_2 denote any of the thermal bath particles. Other reactions are forbidden due to the symmetry we assumed. The abundances of the particles can be calculated by solving a set of N coupled Boltzmann equations,

$$\begin{aligned} a^{-3}\frac{d(n_i a^3)}{dt} = & \sum_{j,B} \langle \sigma_{ij} v\rangle [n_{i,eq} n_{j,eq} - n_i n_j] \\ & +(\langle \sigma'_{ij} v\rangle n_i n_B - \langle \sigma'_{ji} v\rangle n_j n_B) \\ & +\Gamma_{ij}(n_i - n_{i,eq}), \end{aligned} \tag{1.26}$$

where we sum over all possible DS (summation over j) and bath particles (summation over B). We defined the cross sections as follows,

$$\sigma_{ij} = \sigma(\chi_i \chi_j \to B_1 B_2), \tag{1.27}$$
$$\sigma'_{ij} = \sigma(\chi_i B_1 \to \chi_j B_2), \tag{1.28}$$
$$\Gamma_{ij} = \Gamma(\chi_i \to \chi_j B_1 B_2). \tag{1.29}$$

Since χ_1 is the lightest particle and it is stable, all other χ_i particles eventually decay into χ_1. Therefore, it is more relevant to track the quantity $n = \sum_{i=1}^{N} n_i$ where i runs over the DS particles only. If we sum over equations (1.26), we obtain

$$a^{-3}\frac{d(n a^3)}{dt} = \sum_{i,j=1}^{N} \langle \sigma_{ij} v\rangle [n_{i,eq} n_{j,eq} - n_i n_j]. \tag{1.30}$$

We see that due to the summation, the second and third term in eq. (1.26) drop out because cross sections and decay rates remain the same if we reverse the process. The reactions of type (1.23) dominate the freeze-out so we can assume that $\frac{n_i}{n} \approx \frac{n_{i,eq}}{n_{eq}}$. This simplifies eq. (1.30) to,

$$a^{-3}\frac{d(n a^3)}{dt} = \langle \sigma_{eff} v\rangle [n_{eq}^2 - n^2], \tag{1.31}$$

with,

$$\sigma_{eff} = \sum_{i,j=1}^{N} \sigma_{ij} \frac{n_{i,eq}}{n_{eq}} \frac{n_{j,eq}}{n_{eq}}. \tag{1.32}$$

We see that this equation has te same form as eq. (1.9), so we can solve it with the same techniques as in the simple freeze-out mechanism with just one DS particle. It is just more complicated to compute the effective thermally averaged cross section, because it contains more processes. Using equation (1.7), we can approximate $\frac{n_{i,eq}}{n_{eq}}$

if we assume that the DS particles are highly non-relativistic ($m_i \ll T,\ \forall i$),

$$
\begin{aligned}
\frac{n_{i,eq}}{n_{eq}} &= \frac{g_i \left(\frac{m_i T}{2\pi}\right)^{3/2} e^{-m_i/T}}{\sum_{j=1}^{N} g_j \left(\frac{m_j T}{2\pi}\right)^{3/2} e^{-m_j/T}} \\
&= \frac{g_i (m_i + m_1 - m_1)^{3/2}\ e^{-m_i x/m_1}}{\sum_{j=1}^{N} g_j (m_j + m_1 - m_1)^{3/2}\ e^{-m_j x/m_1}} \times \frac{m_1^{3/2} e^x}{m_1^{3/2} e^x} \\
&= \frac{g_i (1+\Delta_i)^{3/2}\ e^{-\Delta_i x}}{\sum_{j=1}^{N} g_j (1+\Delta_j)^{3/2}\ e^{-\Delta_j x}} \\
&= \frac{g_i (1+\Delta_i)^{3/2}\ e^{-\Delta_i x}}{g_{eff}},
\end{aligned}
\tag{1.33}
$$

with $\Delta_i = \frac{m_i - m_1}{m_1}$ and $g_{eff} = \sum_{j=1}^{N} g_j (1+\Delta_j)^{3/2}\ e^{-\Delta_j x}$. With this, the effective cross section becomes

$$
\sigma_{eff} = \sum_{i,j=1}^{N} \sigma_{ij} \frac{g_i g_j}{g_{eff}^2} (1+\Delta_i)^{3/2} (1+\Delta_j)^{3/2}\ e^{-(\Delta_i + \Delta_j)x}. \tag{1.34}
$$

1.4 Dark matter detection

The obvious next step in the DM search was to start up experiments that can detect the DM. In the past decades, there have been three main strategies used by researchers to detect DM interactions with SM particles, assuming of course that DM is a particle itself and interacts in some way with matter. These strategies are shown schematically in figure 1.6. Depending on how we look at this process (where we do not know yet what happens inside the blob), we have to design a specific experiment that can observe it. We quickly review the three main types of experimental strategies that correspond to the three arrows in figure 1.6.

1.4.1 Direct detection

Through the comparison of the motion of stars and the amount of visible mass, scientists observed that around most galaxies, even our own, there is a halo of DM. This means that the earth is flying through this halo and that DM particles are passing right by us constantly. Most DM does not interact with anything, but a small fraction might scatter with atoms. That is why scientist have build detectors to observe the recoil energies of these scattering events. The detectors are typically placed deep underground to shield against cosmic ray backgrounds. Cosmic radiation loses all of its energy before it can reach these underground

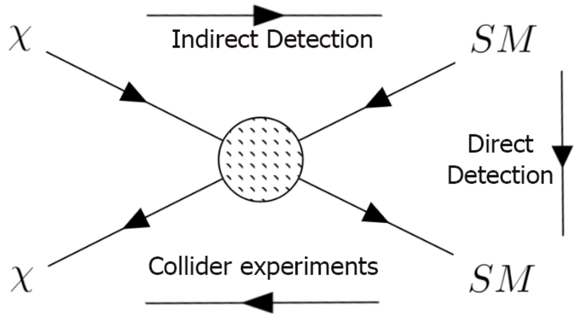

Figure 1.6: A schematic representation of the three main detection strategies for a DM particle.

detectors, but because DM interacts so weakly, it can reach the detector. Of course, the probability that the DM flies through the detector without scattering is still very large, depending on the cross section which we do not know. The predicted interaction rate is typically small, which is why most of these detectors require a large volume, just as in the case with neutrino experiments.

Direct detection experiments can give a lot of information about the interactions (cross section) and the kinematics (mass) of the DM. Unfortunately, no significant amount of scattering events have been observed yet. This gives large constraints on the mass and cross section of specific DM models. For instance, the constraints for WIMPs obtained by the XENON1T experiment [36] are summarized in figure 1.7.

1.4.2 Indirect detection

In addition to detecting the DM particles directly, it is also possible to observe the end products of DM annihilation from regions of increased DM density such a the ones observed in the centre of our galaxy or in dwarf galaxies. Possible signals include antimatter (positrons and anti-protons), gamma rays and neutrinos. These signals are affected by astrophysical processes, which makes the analysis of the data very difficult. This is why the detection of DM has not been confirmed yet even though some interesting fluctuations have already been put forward. For example, in 2008, the positron and anti-proton data from the PAMELA satellite [39] was released. The satellite observed a higher positron flux than would be expected. This excess, later confirmed by AMS [40], could come from these DM annihilation events, but it could also be explained by a number of pulsar as well as secondary production in supernova remnants. This hypothesis has to be tested before a DM detection can be claimed.

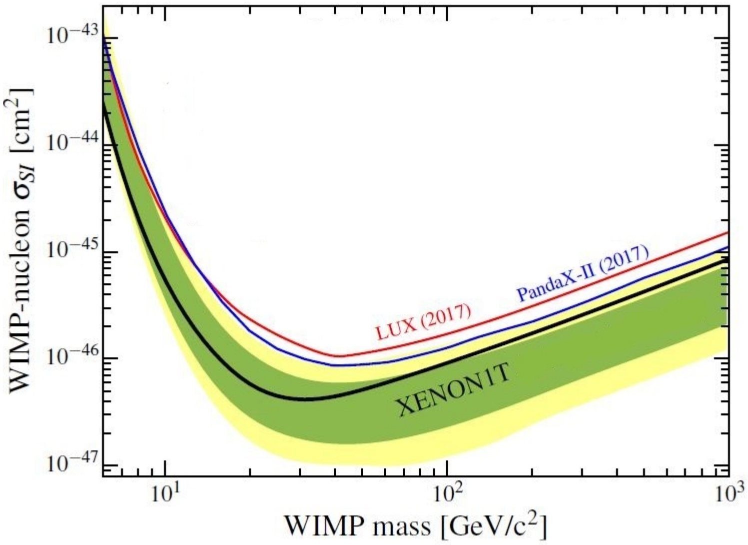

Figure 1.7: The spin-independent WIMP-nucleon cross section σ_{SI} limits as a function of WIMP mass at 90% confidence level (black) for the last run of XENON1T [36]. In green and yellow are the 1 and 2σ sensitivity bands. Earlier results from LUX [37] (red) and PandaX-II [38] (blue) are shown for comparison.

1.4.3 Collider experiments

Classical searches

A third way of trying to detect DM is at accelerator experiments such as the Large Hadron Collider (LHC) at CERN. In such colliders, SM particles are accelerated to very high energies. If they reach a sufficiently high energy, they collide. In these collisions, all SM particles can be produced by various processes. Therefore, detectors are placed around the collision point to detect these particles. In the case of the LHC, several detectors are placed around it of which CMS and ATLAS are the largest and most important ones. If dark matter couples in some way to the standard model, it is even possible to produce it too at LHC. However, since dark matter is assumed to be electrically neutral, it can not be seen by the detectors. Only charged particles leave a signal in the detector. However, if the DM would decay, we could observe its decay products. The only problem with this strategy is that dark matter should be stable or at least have a very long lifetime since it is present in our universe already from the moment the first structures started to form. Thus, if the DM particles would decay, it happens way outside the detector and it is not possible to detect the decay products. Hence, dark matter can only be directly detected as missing energy, just like any other neutral and stable particle. The searches for stable, neutral particles are called mono-X searches [1] and look for visible particles or jets in an event with missing energy. These searches can not distinguish DM from any other neutral and detector-stable particle meaning that the detection of dark matter can not be claimed on the basis of collider data alone. Direct or indirect detection methods provide a way to confirm whether a potential signal is truly dark matter.

The fact that results from collider experiment can not give a complete proof of dark matter does not mean these experiments can not be used to extract information about possible DM candidates. For instance, if there are no DM signals observed, constraints can be put on certain models. As a consequence, there is already a lot of pressure on the WIMP paradigm due to the lack of any sign of dark matter at LHC [41] but also in direct detection experiments.

Collider experiments are not only trying to detect the DM itself, but also other undiscovered particles that potentially mediate the interactions between the DM and SM particles. These particles could be for instance superparticles of the MSSM like squarks or sleptons which are charged and thus can be detected at LHC [42].

Recent strategies

Nowadays, a lot of models that predict new particles exist and therefore, it is hard to test every model at colliders. This has motivated more systematic, model-independent studies which fall mainly into two categories. The first is making use of effective operators describing the low energy interactions between the DM and SM particles. This effective field theory [43] (EFT) approach does not depend on the full theory of the dark sector which is still unknown. However, we can only use the EFT approximation when the energy scale at which the processes happen is smaller than the cut-off scale. An alternative approach that is often used for collider studies is the framework of Simplified models [6]. These are models constructed with a minimal particle content to describe certain signatures of various experiments. Simplified models can be viewed as arising from integrating out the irrelevant particles and taking a certain limit of the more detailed theory, like the Minimal Supersymmetric Standard Model (MSSM). This is how data is interpret very often nowadays in many sorts of experiments, but it is also used to display the complementarity of the various experimental probes. Simplified models have become the main vehicle for interpreting DM searches at LHC, but also for projecting the reach of future colliders and comparing with direct and indirect detection experiments. In the literature, many different simplified models can be found, see [44–46].

Scientists are looking for other ways of producing more exotic signatures in colliders (i.e. other than for instance the missing energy signal) like SM particles that are produced somewhere inside the detector, rather than close to the place where the collision happened. This is referred to as displaced vertices. They can occur when an unknown particle decays to this observed particle and another unknown (potentially DM) particle inside the detector. Therefore, it is needed that this decaying particle has a macroscopic decay, otherwise it would decay immediately after it is produced in the collision. Simplified models of new physics leading to such exotic signatures can be realized by adding two unknown particles to the SM [47]. In the spirit of simplified models, these particles might be a part of a way larger theory with more particles that are neglected for simplicity. In the next chapter, we discuss an example of such a simplified model where one could for instance consider the lightest neutralino coupling only to one of the sleptons and its corresponding lepton. This captures not only the physics of the MSSM, but of all models where DM couples to a charged scaler.

Chapter 2

Simplified model for co-annihilations

As we have discussed in section 1.3, there are a couple of ways the DM could have been produced in the early universe, depending on the nature of the DM and other dark sector particles. Already many searches, for instance at the LHC, have been performed to try to detect the WIMP which is produced via the freeze-out mechanism. Unfortunately, no experimental signals have been found yet meaning that these searches are putting a lot of pressure on the WIMP paradigm. Therefore, it is necessary to look at other possible production mechanisms. In this chapter, we introduce a simplified model inspired by supersymmetry and study how the DM candidate in this model can be produced. This DM candidate couples to one of the superpartners of the fermions called the sfermions. How these particles couple is discussed in section 2.1. After this, we look at how the DM abundance can evolve in our model. To do this, we have to solve the complete Boltzmann equation including all possible processes influencing the dark sector abundances. These processes are discussed in section 2.2 where we also look at the Boltzmann equation that describes the evolution of the DM abundance. A more detailed study of how all the different processes can influence the DM relic abundance is done in section 2.3. This largely depends on the value of the coupling constant that drives the interactions between the DM and sfermion it couples to. For large values of this coupling, we retrieve the same solution as the standard freeze-out mechanism[1], but decreasing the coupling changes the behaviour and other effects start to play a role.

---

[1] When multiple dark sector particles play a role, we are in the co-annihilation regime. However, we will still refer to this as the standard freeze-out mechanism since the working principle is the same. If we apply the equations we derived for co-annihilations in section 1.3.3 on just one particle, we retrieve the equations for the freeze-out mechanism for just one particle we derived in section 1.3.1

2.1 The model

Let us start by introducing the most important particle of our model, the DM candidate. Here, we consider a Majorana fermion which we denote by χ. The main difference between a Majorana and Dirac fermion is that a Majorana fermions is its own anti-particle (in the SM, all fermions are Dirac, except for the neutrinos of which we do not know the nature yet [48]). Its kinetic and mass term in the Lagrangian are

$$\mathcal{L}_{DM} = \frac{i}{2}\bar{\chi}\gamma^\mu \partial_\mu \chi - \frac{m_\chi}{2}\bar{\chi}\chi. \tag{2.1}$$

From this, we see that χ does not couple to any of the gauge bosons directly. In our model, it only interacts with the fermions (leptons and quarks). The interactions are mediated by another new dark sector particles, a charged scalar $\widetilde{f}$. The Lagrangian that governs these processes and the interactions of this scalar with the other SM particles is

$$\mathcal{L}_{int} = (D_\mu \widetilde{f})^\dagger \; D^\mu \widetilde{f} \;-\; \lambda_\chi \widetilde{f}\bar{f}\frac{1-\gamma_5}{2}\chi \;+\; h.c. \tag{2.2}$$

Here, f denotes one of the SM fermions and D_μ denotes the covariant derivative which contains all the interactions with $\widetilde{f}$ and the SM gauge bosons. The quantum numbers of $\widetilde{f}$ are defined to be the same as the corresponding fermion. The second term in the Lagrangian describes the yukawa interactions between the DS and SM particles, where λ_χ is the yukawa coupling constant. In the MSSM, such yukawa interactions appear with the charged scalar $\widetilde{f}$ being the superpartner of the fermion f named the sfermion. Therefore, we will refer to the charged scalar as the sfermions, although we are only considering a simplified model, not the full MSSM. There, all the superpartners of the fermions would be present with each of them having their own coupling constant λ_χ that would be fixed by supersymmetry. We do not sum over all possible fermions, only one at a time will couple such that we have two dark sector particles with a free coupling constant. In the Lagrangian can be seen that only the right handed fermions couple to χ due to the presence of the projection operator. The left handed ones do not interact directly with χ and are therefore not considered in this model.

Dark matter has been present in our universe almost since the beginning of its existence. Thus, for χ to be a viable DM candidate, is should be stable. If we assume that the DM mass m_χ is less than the one of the sfermion $m_{\widetilde{f}}$, then χ will not be able to decay to $\widetilde{f}$. However, it is still possible that the DM decays to two or more lighter SM particles. To prevent this, we impose a $\mathbb{Z}_2$-symmetry. Under this symmetry, all SM particles are even. Only the DS particles χ and $\widetilde{f}$ are odd. This makes that if a DS particle decays, it must decay to at least one other DS particle, otherwise it breaks the symmetry. Due to this, the lightest DS particle, which in our case will be χ, is stable.

On top of the gauge and Yukawa interactions between the DS en SM particles, it is also possible to have a Higgs-portal interaction given by

$$\mathcal{L}_H = \lambda_H H^\dagger H \widetilde{f}^\dagger \widetilde{f}. \tag{2.3}$$

This type of interactions do not involve the DM, but it could influence the annihilation rate of $\widetilde{f}$. The extent of the influence depends on the coupling λ_H. We assume in this thesis that such coupling is enough small to not interfere in the dynamics leading to the relic DM abundance. We leave the study of effects when this type of coupling does interfere for the future.

Now that we have defined the simplified model, we are interested in the free parameters of the model. First of all, we already mentioned that the coupling constant λ_χ will not be fixed. Also the masses of both χ and $\widetilde{f}$ do not have fixed values. The only restrictions is that the mass of χ has to be lower than the mass of $\widetilde{f}$ to keep the DM particle stable. Thus, we have three free parameters in our model, m_χ, $m_{\widetilde{f}}$ and λ_χ. For this thesis, we will further focus on the region in parameter space where the mass difference $\Delta m = m_{\widetilde{f}} - m_\chi$ between the sfermions and DM is very small such that co-annihilation effects are important. Therefore, we will make use of the parameters

$$m_\chi, \Delta m, \lambda_\chi. \tag{2.4}$$

Depending on the values of the coupling constant λ_χ, the mechanism of producing DM can be very different. In the next sections of this chapter, we discuss the possible cases in more detail.

2.2 Conversion driven freeze-out

The model we introduced in the previous section has two new or dark sector particles, the dark matter candidate χ and a partner that mediates the interactions between χ and the SM particles. We named this particle the sfermion $\widetilde{f}$ which is the superpartners of one of the fermions. From now on, we mainly focus on the case where $\widetilde{f}$ is the superpartner of one of the leptons, i.e. we consider $\widetilde{f} = \widetilde{l}$. This means that the leptons are the only SM particles χ couples to, hence we name it leptophilic dark matter. The case for the squarks (superpartners of the quarks) is very similar but has already been studied in the literature. Therefore, we are only interested in the slepton case. For more details on the squarks, we refer to appendix A or to the literature [49, 50].

In section 1.3, we saw that we can calculate the relic DM density through some kind of mechanism called freeze-out. This was first described for one particle

initial state		final state		scaling
χ	χ	l	$\bar{l}$	λ_χ^4
χ	$\widetilde{l}$	l	γ, Z, H	λ_χ^2
		W^-	ν_l	
$\widetilde{l}$	$\widetilde{l}^\dagger$	γ, Z, W^+	γ, Z, W^-	λ_χ^0
		q	$\bar{q}$	
		H	Z	
		e^-, μ^-, τ^-	e^+, μ^+, τ^+	
$\widetilde{l}$	$\widetilde{l}$	l	l	λ_χ^4

Table 2.1: List of all included co-annihilation processes where l is one of the leptons (e, μ, τ), depending on the case we are studying. Also the dependence of the cross section on the coupling constant λ_χ is denoted in the last column. The $\widetilde{ll}^\dagger$ annihilation into $l\bar{l}$ also has contributions scaling with λ_χ^2 and λ_χ^4.

species, but later generalized for more. In this scenario, all the dark sector particles were initially in chemical equilibrium with the SM particles through efficient co-annihilation processes of which the rate Γ is larger than the Hubble rate H. At a given time, the co-annihilation processes would cease to be efficient and the DS particles would decouple. In our model, χ and $\widetilde{l}$ co-annihilate via the processes that are listed in table 2.1. If these processes are of the same order of the weak interactions, they were efficient in the early universe and we can use the freeze-out mechanism to determine the relic DM abundance. The dependence on the coupling λ_χ is also denoted in table 2.1. We see that the annihilation processes of $\widetilde{l}$, $\widetilde{ll}^\dagger \leftrightarrow SM\ SM$ do not depend on λ_χ. Only weak interactions play a role here making that the sleptons were initially in equilibrium. The other co-annihilation processes including χ do depend on the coupling meaning that they could be initially inefficient for low values of λ_χ (more on this in section 2.3.2). However, we can still use the freeze-out mechanism if the conversion processes $\widetilde{l} \leftrightarrow \chi$ like the ones in figure 2.1 are efficient such that the DM is still in equilibrium through its mediator. As long as the conversion processes are efficient such that chemical equilibrium holds between χ and $\widetilde{l}$, we do not have to include them in the Boltzmann equation. We obtain the correct result by taking into account only the co-annihilation processes and by assuming that χ is initially in chemical equilibrium.

initial state		final state		scaling
χ	l	$\widetilde{l}$	γ, Z, H	λ_χ^2
	γ, Z, H		$\bar{l}$	
	W^-		$\bar{\nu}_l$	
	ν_l		W^+	
$\widetilde{l}$		χ	l	λ_χ^2
χ	χ	$\widetilde{l}$	$\widetilde{l}^\dagger$	λ_χ^4

Table 2.2: List of all included conversion processes and their dependence of the cross section on λ_χ. l is one of the leptons (e, μ, τ), depending on the case we are studying.

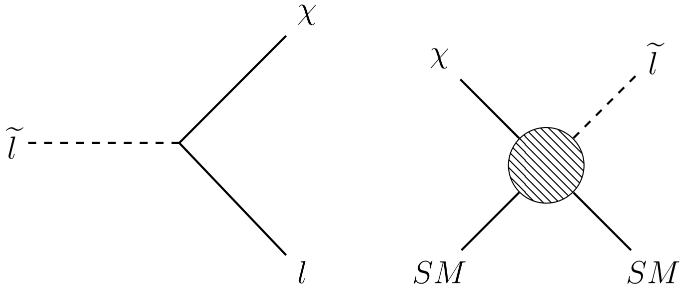

(a)　(b)

Figure 2.1: The Feynman diagrams for the most important conversion processes.

In our model, the conversion processes that are all listed in table 2.2 depend on the coupling constant λ_χ. This means that when this coupling is large enough such that the conversion rates are larger than the Hubble rate H, we can use the standard freeze-out mechanism. However, we would like to consider arbitrary values for λ_χ. Thus, in order to solve for the relic abundance in general, we need to solve the Boltzmann equation that takes into account all the conversion processes. In particular, we have

$$\begin{aligned}\frac{dY_\chi}{dx} = \frac{-s}{Hx}\Bigg[&\langle\sigma_{\chi\chi}v\rangle\left(Y_\chi^2 - Y_{\chi,eq}^2\right) + 2\langle\sigma_{\chi\widetilde{l}}v\rangle\left(Y_\chi Y_{\widetilde{l}} - Y_{\chi,eq}Y_{\widetilde{l},eq}\right)\\ &+ \frac{2\Gamma_{\chi\to\widetilde{l}}}{s}\left(Y_\chi - Y_{\widetilde{l}}\frac{Y_{\chi,eq}}{Y_{\widetilde{l},eq}}\right) - \frac{2\Gamma_{\widetilde{l}}}{s}\left(Y_{\widetilde{l}} - Y_\chi\frac{Y_{\widetilde{l},eq}}{Y_{\chi,eq}}\right)\\ &+ \langle\sigma_{\chi\chi\to\widetilde{l}\widetilde{l}^\dagger}v\rangle\left(Y_\chi^2 - Y_{\widetilde{l}}^2\frac{Y_{\chi,eq}^2}{Y_{\widetilde{l},eq}^2}\right)\Bigg], \qquad (2.5)\end{aligned}$$

$$\begin{aligned}\frac{dY_{\widetilde{l}}}{dx} = \frac{-s}{Hx}\Bigg[&\langle\sigma_{\widetilde{l}\widetilde{l}^\dagger}v\rangle\left(Y_{\widetilde{l}}^2 - Y_{\widetilde{l},eq}^2\right) + 2\langle\sigma_{\chi\widetilde{l}}v\rangle\left(Y_\chi Y_{\widetilde{l}} - Y_{\chi,eq}Y_{\widetilde{l},eq}\right)\\ &- \frac{2\Gamma_{\chi\to\widetilde{l}}}{s}\left(Y_\chi - Y_{\widetilde{l}}\frac{Y_{\chi,eq}}{Y_{\widetilde{l},eq}}\right) + \frac{2\Gamma_{\widetilde{l}}}{s}\left(Y_{\widetilde{l}} - Y_\chi\frac{Y_{\widetilde{l},eq}}{Y_{\chi,eq}}\right)\\ &- \langle\sigma_{\chi\chi\to\widetilde{l}\widetilde{l}^\dagger}v\rangle\left(Y_\chi^2 - Y_{\widetilde{l}}^2\frac{Y_{\chi,eq}^2}{Y_{\widetilde{l},eq}^2}\right)\Bigg], \qquad (2.6)\end{aligned}$$

where $Y_{\widetilde{l}}$ is the summed contribution over the sleptons and the anti-sleptons. Therefore, we need to multiply some of the thermally averaged cross sections and decay rates by two to account for the same processes that happen with the anti-sleptons instead of the sleptons. The thermally averaged co-annihilation cross sections include all processes that are denoted in table 2.1. They are defined as

$$\langle\sigma_{\chi\chi}v\rangle = \sum_{i,j}\langle\sigma_{\chi\chi\to ij}v\rangle, \qquad (2.7)$$

$$\langle\sigma_{\chi\widetilde{l}}v\rangle = \sum_{i,j}\langle\sigma_{\chi\widetilde{l}\to ij}v\rangle, \qquad (2.8)$$

$$\langle\sigma_{\widetilde{l}\widetilde{l}}v\rangle = \sum_{i,j}\langle\sigma_{\widetilde{l}\widetilde{l}\to ij}v\rangle, \qquad (2.9)$$

where i, j denote SM particles. For the conversion processes $\chi\ SM \leftrightarrow \widetilde{l}\ SM$ in table 2.2, the interaction rate is defined as

$$\Gamma_{\chi\to\widetilde{l}} = \sum_{i,j}\langle\sigma_{\chi i\to\widetilde{l}j}v\rangle n_{i,eq}, \qquad (2.10)$$

where i, j again represent SM particles.

2.3 Relevant processes influencing the abundance

2.3.1 Calculating the cross sections and decay rate

If we want to solve the system of coupled Boltzmann equations (equations (2.5) and (2.6)), we need to calculate first all thermally averaged cross sections and decay rates. To facilitate this, we make use of specialized software. First, we implement the model we defined in section 2.1 into FeynRules [51], a package that allows us to calculate the Feynman rules for all tree level diagrams. Knowing the Feynman rules, the amplitude squared $|\mathcal{M}|^2$ can be found analytically by using another software package called CalcHEP [52]. FeynRules provides the input files CalcHEP needs to generate $|\mathcal{M}|^2$. For all $2 \to 2$ processes in table 2.1 and 2.2, we can now calculate the thermal averaged cross section which is defined in equation (1.8) and can be simplified to

$$\langle \sigma_{ij} v \rangle n_{i,eq} n_{j,eq} = \frac{g_i g_j}{256\pi^5} T \int \frac{p_{ij} p_{ab}}{\sqrt{s}} |\mathcal{M}|^2 K_1\left(\frac{\sqrt{s}}{T}\right) ds \; d\cos\theta, \tag{2.11}$$

where K_i denotes a modified Bessel function of the second kind and p_{ij} and p_{ab} are the absolute values of the three momenta of respectively the initial and final state in the centre-of-mass (COM) frame. Because CalcHEP gives us an analytic expression of the matrix element squared as a function of the Mandelstam variables s and t, we rewrite this integral using [53]

$$t = (E_{ij} - E_{ab})^2 - (p_{ij} - p_{ab})^2 - 4 p_{ij} p_{ab} \sin^2\left(\frac{\theta}{2}\right). \tag{2.12}$$

The integration becomes,

$$\langle \sigma_{ij} v \rangle n_{i,eq} n_{j,eq} = \frac{g_i g_j}{512\pi^5} T \int \frac{|\mathcal{M}|^2}{\sqrt{s}} K_1\left(\frac{\sqrt{s}}{T}\right) ds \; dt. \tag{2.13}$$

The integration limits for t can be found by filling in $\theta = 0$ and $\theta = \pi$ in equation (2.12). Now we can use Mathematica to do the integration of $|\mathcal{M}|^2$ over t analytically. The integration over the COM energy s is too difficult to perform analytically by Mathematica due to the Bessel function in the integrand. This means that this integration has to be done numerically. In this process, there appear a number of numerical problems. Our methods used to treat these issues can be found in appendix B.

Besides the $2 \to 2$ processes of which we have already obtained the thermally averaged cross section, there is also the decay of the slepton $\widetilde{l} \to \chi l$ that influences the evolution of the yield. For this process, we need to calculate the decay width Γ via [53]

$$\Gamma = \frac{1}{32\pi^2} \int |\mathcal{M}|^2 \, \frac{p_{ab}}{m_{\widetilde{f}}} \, d\Omega. \tag{2.14}$$

To solve the Boltzmann equations, we need the thermally averaged decay rate, which is defined as

$$\Gamma_{\widetilde{f}} \equiv \Gamma\langle\gamma^{-1}\rangle = \Gamma\frac{K_1\left(m_{\widetilde{f}}/T\right)}{K_2\left(m_{\widetilde{f}}/T\right)}, \tag{2.15}$$

where γ is the Lorentz factor and the brackets denote as usual the thermal average. In the last equality, we ignored quantum statistical corrections and just assumed a Boltzmann distribution. Now we have all the necessary ingredients to solve the Boltzmann equation. To check that our own code reproduces the correct relic abundance, we fixed our set of free parameters (equation 2.4) such that we are in the standard freeze-out regime. There are some software packages such as micrOMEGAs [54] that can calculate the relic abundance in this regime too. We implemented the model under study here in micrOMEGAs with the same set of parameters in order to compare the results. We found that both tools reproduces more or less the same relic abundance[2].

2.3.2 Comparison between the processes

In section 2.1, we mentioned that the model we introduced has three free parameters, the DM mass m_χ, the mass-splitting Δm between the DM and its co-annihilation partner and the coupling λ_χ between the two, see equation (2.4). In this section, we inspect the influence of this coupling on the conversion and co-annihilation rates together with the influence on the evolution of the DM yield. Therefore, the behaviour in four regimes characterized by the value of the coupling is investigated while the DM mass and the mass splitting are kept fixed ($m_\chi = 150$ GeV and $\Delta m = 5$ GeV). For this comparison, the co-annihilation partner is $\widetilde{\tau}$. The analysis for $\widetilde{\mu}$ and $\widetilde{e}$ is qualitatively the same. We already summarize the main points of the discussion below in table 2.3.

Regime 1: Freeze-out with co-annihilation ($\lambda_\chi \sim 10^{-1}$)

We start in the regime where the coupling constant is rather large, of the order of 0.1. From table 2.1 and 2.2, we see that almost all processes relevant to compute the DM abundance depend on λ_χ, except for the $\widetilde{\tau}$ annihilation processes. For this coupling of the same order of the one of the weak interactions, we expect that conversion rates are initially way larger than the Hubble rate. To check this, we can take a look at figure 2.2a where we plotted the rates $\Gamma = \langle\sigma v\rangle n$ of all the relevant processes. How these rates are defined is reported in appendix C. In this figure, we see that initially, all processes are efficient. The red lines denote the conversion

---

[2] There are small numerical differences which account for the small discrepancy of about 5%.

	Name of the regime	Most imporant processes	Value of λ_χ
1	Freeze-out with co-annihilations	$\chi\chi \leftrightarrow SM\ SM$ $\chi\widetilde{\tau} \leftrightarrow SM\ SM$ $\widetilde{\tau}\widetilde{\tau}^\dagger \leftrightarrow SM\ SM$	10^{-1}
2	Freeze-out driven by $\widetilde{\tau}\widetilde{\tau}^\dagger$ annihilation	$\widetilde{\tau}\widetilde{\tau}^\dagger \leftrightarrow SM\ SM$	10^{-5}
3	Conversion-driven freeze-out	$\widetilde{\tau}\widetilde{\tau}^\dagger \leftrightarrow SM\ SM$ $\chi \leftrightarrow \widetilde{\tau}$	$5 \cdot 10^{-7}$
4	Freeze-in	$\widetilde{\tau} \to \chi l$	10^{-8}

Table 2.3: A summary of all the regimes with their important processes. The values of λ_χ that are shown are taken as benchmarks. Larger ranges of λ_χ are associated with the regimes.

processes and we see that especially for the processes $\widetilde{\tau} \leftrightarrow \tau\chi$ and $\chi\ SM \leftrightarrow \widetilde{\tau}\ SM$, the rate stays well above the Hubble rate for a long time compared to the other rates. Due to these processes, χ and $\widetilde{\tau}$ are in chemical equilibrium which means that the standard freeze-out mechanism yields the correct answer. Also, the co-annihilation rates (blue lines in figure 2.2a) are larger than the Hubble rate for large temperatures ($x = \frac{m_\chi}{T} < 30$) meaning that our two co-annihilation partners are initially in thermal contact with the bath particles. Looking at the evolution of the yield in figure 2.2b, the same behaviour is visible. Until $x \approx 30$ the yield for both χ and $\widetilde{\tau}$ follow their equilibrium values until they decouple at approximately the same time, when the co-annihilation rates drop below the Hubble rate. From then on, we see that the abundance of χ freezes out while the $\widetilde{\tau}$ keeps decaying.

Regime 2: Freeze-out driven by $\widetilde{\tau}\widetilde{\tau}^\dagger$ annihilation ($\lambda_\chi \sim 10^{-5}$)

As we expected, for a coupling of the order of the weak coupling constant, we retrieve the same results as the standard freeze-out mechanism. Now we can inspect what happens if we go to a regime with a smaller coupling constant. We expect that all the rates depending on λ_χ decrease. And this is exactly what happens in figure 2.3a. The annihilation rate of $\widetilde{\tau}\widetilde{\tau}^\dagger$ stays at the same level, all the others decrease. Two out of the three conversion processes still are larger than the Hubble rate keeping χ in equilibrium with $\widetilde{\tau}$ meaning that we can still use the standard freeze-out mechanism to calculate the final DM relic abundance. However, when we look at the blue curves for the co-annihilation processes, we see

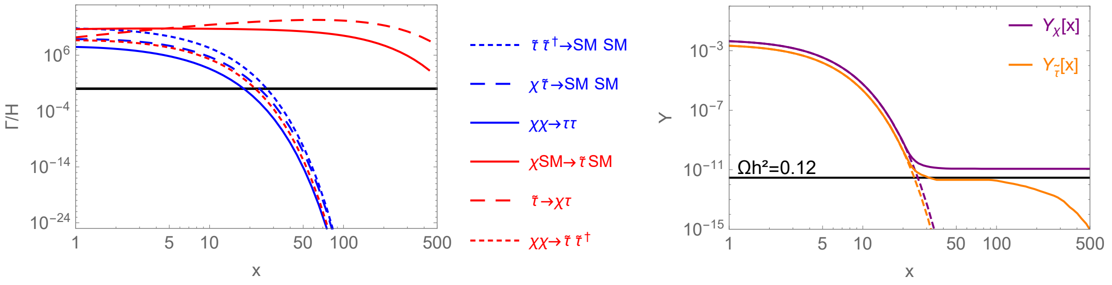

(a)

(b)

Figure 2.2: LEFT: All the rates compared to the Hubble constant as a function of $x = \frac{m_\chi}{T}$. The conversion processes are depicted in red, the co-annihilation ones in blue. The Black line depicts where $\Gamma = H$. RIGHT: The evolution of the yield of χ (solid purple line) and $\widetilde{\tau}$ (solid orange line) and their equilibrium yield (dashed lines) as a function of temperature. Both figures are calculated with the following parameters: $m_\chi = 150$ GeV, $\Delta m = 5$ GeV and $\lambda_\chi = 10^{-1}$, i.e. we are in the freeze-out regime with co-annihilations. More details on the exact definitions of the rates can be found in appendix C.

that the one depicting the annihilation of $\chi\chi$ into SM particles is so low, that it does not play a role. Even the co-annihilation rate for $\chi\widetilde{\tau} \leftrightarrow SM\ SM$ is initially of the same order of H, but decreases very fast. Therefore, only one process influences the relic DM abundance, namely the annihilation of $\widetilde{\tau}$ into SM particles $\widetilde{\tau}\widetilde{\tau}^\dagger \leftrightarrow SM\ SM$. It dominates the other two completely. This is also the only process that does not depend on our coupling constant λ_χ. Because all processes depending on λ_χ do not influence the DM abundance, we may conclude that in this regime, the calculated relic abundance is always the same regardless of the precise value of the coupling. We can vary it within the regime, the calculated result will not change.

In figure 2.3b, we can find almost the same evolution of the yield as in the previous regime, although some of the co-annihilation processes are suppressed here. Just as in the previous case, the $\widetilde{\tau}\widetilde{\tau}^\dagger$ annihilation is the dominating process. Therefore, changing the coupling constant changed the final abundance only a little bit. One thing that we might expect to happen is that χ would decouple way earlier because of the small annihilation and co-annihilation rates. Due the still efficient conversion processes, χ stays in equilibrium with $\widetilde{\tau}$ which at his turn is coupled to the thermal bath because the annihilation of $\widetilde{\tau}$ does not depend on λ_χ and is efficient in every regime. Therefore, both particles still decouple at the same time, at $x \approx 30$.

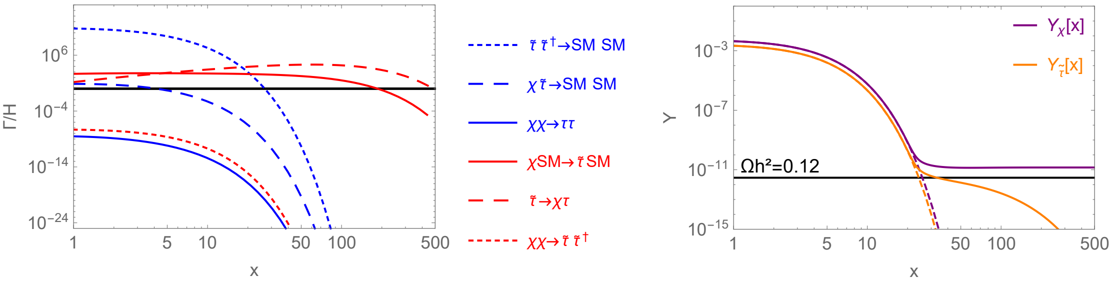

(a) (b)

Figure 2.3: LEFT: All the rates compared to the Hubble constant as a function of $x = \frac{m_\chi}{T}$. The conversion processes are depicted in red, the co-annihilation ones in blue. The Black line depicts where $\Gamma = H$. RIGHT: The evolution of the yield of χ (solid purple line) and $\tilde{\tau}$ (solid orange line) and their equilibrium yield (dashed lines) as a function of temperature. Both figures are calculated with the following parameters: $m_\chi = 150$ GeV, $\Delta m = 5$ GeV and $\lambda_\chi = 10^{-5}$, i.e. we are in the freeze-out regime driven by $\tilde{\tau}\tilde{\tau}^\dagger$ annihilation.

Regime 3: Conversion-driven freeze-out ($\lambda_\chi \sim 5 \cdot 10^{-7}$)

As we have been lowering the coupling, we have seen that the assumptions that χ and $\tilde{\tau}$ are in equilibrium is not that obvious. For an even lower coupling, the assumption might break down. This is exactly what happens. For $\lambda_\chi \sim 5 \cdot 10^{-7}$, we enter a regime where the ratio of the conversion and Hubble rate is very close to or even smaller than one, as can be seen in figure 2.4a. We finally arrived in the zone where we can not use the standard freeze-out mechanism. In the previous regimes, the solution of the Boltzmann equation in section 1.3.3 would always yield the same result as the solutions of the full set of Boltzmann equations we presented in section 2.2. From now on, this is not the case and we must solve the full set of Boltzmann equations where all processes in table 2.1 and 2.2 are taken into account explicitly. We can see in figure 2.4a that not every process is equally important. At early times, the annihilation of $\tilde{\tau}$ is again the dominant process. Now, not only the DM annihilation ($\chi\chi \leftrightarrow SM\ SM$) and co-annihilation ($\chi\tilde{\tau} \leftrightarrow SM\ SM$) processes are inefficient, also the conversion processes are on the edge of being efficient. Therefore, χ loses contact with all the other particles which makes it leave equilibrium almost immediately[3]. We can clearly see the DM yield deviating from its equilibrium value in figure 2.4b, where it is also noticeable that the yield of χ still stays close the $\tilde{\tau}$-yield until they both decouple from the thermal bath. This is due to barely but still efficient conversion processes. The

---

[3] This also raises the question if assuming that $Y_\chi(1) = Y_{\chi,eq}(1)$ is still valid. More on this in section 2.4

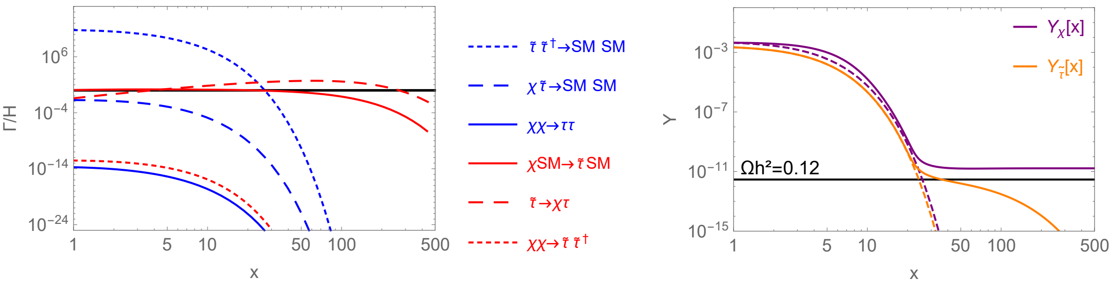

(a) (b)

Figure 2.4: LEFT: All the rates compared to the Hubble constant as a function of $x = \frac{m_\chi}{T}$. The conversion processes are depicted in red, the co-annihilation ones in blue. The Black line depicts where $\Gamma = H$. RIGHT: The evolution of the yield of χ (solid purple line) and $\widetilde{\tau}$ (solid orange line) and their equilibrium yield (dashed lines) as a function of temperature. Both figures are calculated with the following parameters: $m_\chi = 150$ GeV, $\Delta m = 5$ GeV and $\lambda_\chi = 5 \cdot 10^{-7}$, i.e. we are in the conversion-driven freeze-out regime.

decay rate of $\widetilde{\tau}$ (red dashed line in figure 2.4a) grows a bit for larger values of x. Therefore, the χ-yield gets dragged down towards its equilibrium value without reaching it because the conversion processes are not efficient enough.

Regime 4: Freeze-in ($\lambda_\chi \sim 10^{-8}$)

For all the previous regimes, there was some time in the evolution of the universe where the conversion processes were efficient, although sometimes just barely. However, for really low values of the coupling, we would expect that this does not occur any more. In figure 2.5a, the conversion rates for $\lambda_\chi = 10^{-8}$ are always smaller than the Hubble rate. Thus, the evolution of the stau can only slightly influence the DM abundance, but not enough to consider them in equilibrium. In figure 2.5b, where the evolution of the yield is shown, the assumption was made that we start out with a negligible amount of dark matter. In section 2.4, we explain why we make this assumptions and not that the co-annihilation partners are initially in equilibrium as we did before. If we assume initially a negligible amount of DM, we see that the yield rises up to a certain value and from then on, it stays constant. This is exactly the behaviour from the freeze-in mechanism we discussed in section 1.3.2, were we made the same assumption concerning the initial abundance. From this, we can conclude that for these small values of the coupling, the co-annihilation partner does not play an important role in calculation the relic DM abundance. The only importance of the stau here is that it provides a way to produce χ at early times through its decay $\widetilde{\tau} \to \chi\tau$ and the

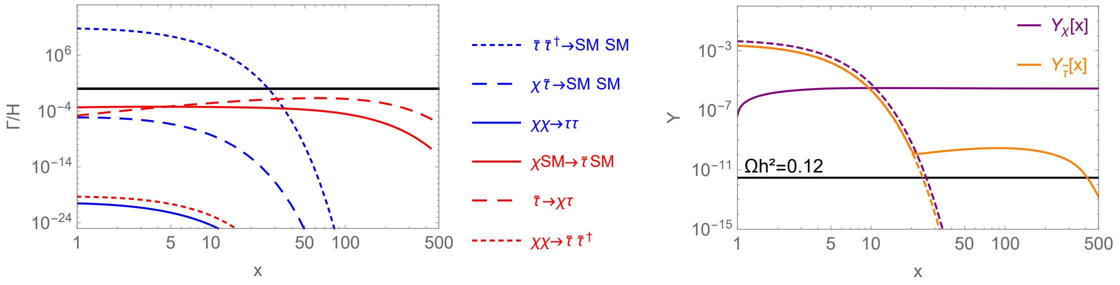

(a) (b)

Figure 2.5: LEFT: All the rates compared to the Hubble constant as a function of $x = \frac{m_\chi}{T}$. The conversion processes are depicted in red, the co-annihilation ones in blue. The Black line depicts where $\Gamma = H$. RIGHT: The evolution of the yield of χ (solid purple line) and $\tilde{\tau}$ (solid orange line) and their equilibrium yield (dashed lines) as a function of temperature. Both figures are calculated with the following parameters: $m_\chi = 150$ GeV, $\Delta m = 5$ GeV and $\lambda_\chi = 10^{-8}$, i.e. we are in the freeze-in regime.

other conversion process. For larger values of x, these processes are not efficient enough to drag down the DM abundance towards its equilibrium value as was the case in the previous regimes. Therefore, once it reached its maximal value, it stays constant.

We now studied all the relevant regimes in which the coupling constant has different values. In table 2.3, we summarized the important processes for every regime. The freeze-out regime with co-annihilations has already been studied extensively in the literature in the context of the WIMP [1, 35, 46, 59]. Already many attempts have been made to discover the WIMP, but as we discussed in section 1.4, no conclusive results have been found yet. Therefore, we will study in the next chapter in which region in the $m_\chi - \Delta m$ plane the standard freeze-out mechanism fails to reproduce the correct relic DM abundance.

2.4 Dependence on initial conditions

A very interesting feature of the freeze-out mechanism is that it does not depend on the initial conditions. For small values of x ($x \gtrsim 1$), the annihilation rates are efficient and therefore, the yield always converges to the equilibrium value, regardless whether we start with zero or with a very high abundance. This is very useful because in general, we do not know yet how the abundance is set in the first moments after the big bang ($x < 1$). For instance inflation or the reheating

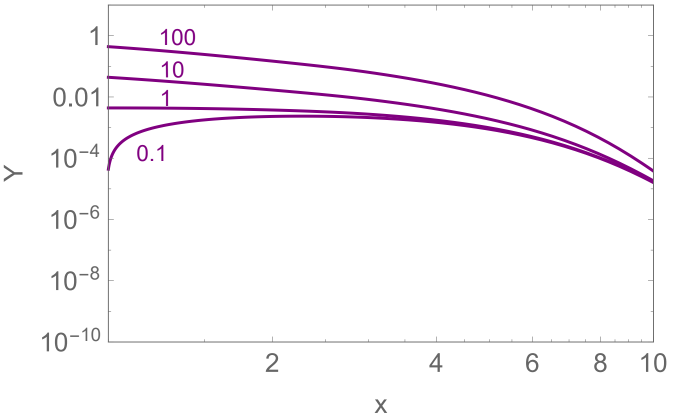

Figure 2.6: Solution of the Boltzmann equation for different initial conditions: $Y_\chi[1] = i \cdot Y_{\chi,eq}$ with $i \in \{0.1, 1, 10, 100\}$. All different solutions are calculated with $\widetilde{\tau}$ as the co-annihilation partner and for the following parameters: $m_\chi = 150$, $\Delta m = 5$ and $\lambda_\chi = 5 \cdot 10^{-7}$, i.e. we are in the conversion-driven freeze-out regime.

processes can influence the DM abundance in a way we do not know [60]. On the other hand, scenarios with a very small coupling do suffer from this. In section 1.3.2 where we introduced the freeze-in mechanism, we explicitly assumed that none of these processes influenced the abundance such that we could start our analysis with a negligible amount of DM. There is no physical reason to state this as a fact. Therefore, production mechanisms are more "reliable" if they do not depend on the initial conditions and we do not have to worry about what happens before.

For the first three regimes in section 2.3.2, we used the fact that $\widetilde{\tau}$ and χ where in chemical equilibrium with the bath particles as an initial condition to solve the Boltzmann equation. This is definitely valid for large values of the coupling ($\lambda_\chi \geq 10^{-5}$ in the $\widetilde{\tau}$ case) because then, the $\widetilde{\tau}$ annihilation process $\widetilde{\tau}\widetilde{\tau}^\dagger \leftrightarrow SM\ SM$ and conversion processes $\widetilde{\tau} \leftrightarrow \chi$ are highly efficient. As can be seen in figure 2.4a in section 2.3.2, for smaller values of the coupling, only the annihilation of $\widetilde{\tau}$ is highly efficient and that is why χ decouples almost immediately from the thermal bath as we can see in figure 2.4b. It seems that the only reason χ starts in equilibrium is because we assumed it. Maybe choosing different initial conditions might result in a different relic abundance. To check this, we plotted the solution of the Boltzmann equation for the same parameters and only changed the initial conditions, see figure 2.6. The three solutions converge relatively fast. This means that there is no dependence on the initial conditions for this value of λ_χ and we can still assume chemical equilibrium as an initial condition. Now we can ask ourself the question: "why does the yield converge if we start from different initial

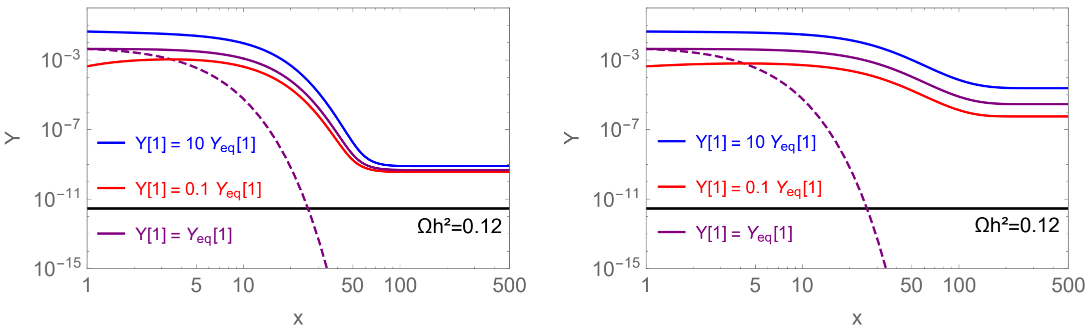

(a) $\lambda_\chi = 2 \cdot 10^{-7}$ (b) $\lambda_\chi = 10^{-7}$

Figure 2.7: Plotting the evolution of the yield for different initial conditions: $Y_\chi[1] = i \cdot Y_{\chi,eq}[1]$ with $i \in \{0.1, 1, 10\}$. Both figures are calculated with $\widetilde{\tau}$ as the co-annihilation partner and for the parameters $m_\chi = 150$ GeV and $\Delta m = 5$ GeV but for two different values of the coupling, $\lambda_\chi = 2 \cdot 10^{-7}$ (left) and $\lambda_\chi = 10^{-7}$ (right). The dashed lines denote the equilibrium yield.

conditions?" The answer can again be seen in figure 2.4a. For small values of x, we see that the conversion process $\chi\ SM \leftrightarrow \widetilde{\tau}\ SM$ is still efficient, although just barely. Due to the efficiency of this process, the dependence of the initial conditions can be washed away. If the processes are highly efficient ($\Gamma \gg H$), the convergence will be fast. For a coupling of the order of $\lambda\chi \sim 5 \cdot 10^{-7}$, i.e. when the conversion process is just barely efficient, it will take some time until they converge.

We would expect that if the ratio $\frac{\Gamma}{H}$ is initially smaller than 1, there will be no more convergence. This again can be checked by going to smaller couplings and solving the Boltzmann equation for different initial conditions. In figure 2.7a, we see that for $\lambda_\chi = 2 \cdot 10^{-7}$, the solutions do seem to come closer, but only at $x \approx 50$. The reason for this is that the process $\widetilde{\tau} \leftrightarrow \chi\tau$ becomes efficient at this temperature (see in figure 2.8a), while all the other conversion processes are never efficient. Going to a coupling of 10^{-7} tough, this effect of conversion does not occur any more. In figure 2.8b, we see that the conversion rates are smaller than the Hubble rate for almost all times. There is just a small window where $\Gamma > H$ for the process $\widetilde{\tau} \leftrightarrow \chi\tau$ and the abundance is dragged down, but this window is not large enough to let the curves for different initial conditions converge and thus, they just run parallel to each other as can be seen in figure 2.7b. As a result, the evolution of the abundance is very dependant on the initial value in this regime. This makes that we cannot just pick a value for Y_χ to start with.

However, we can make an assumption about the initial condition. For instance, we can assume that for $x < 1$, there are no mechanisms that could influence the DM abundance like a coupling to the inflaton [61] or other types of processes with

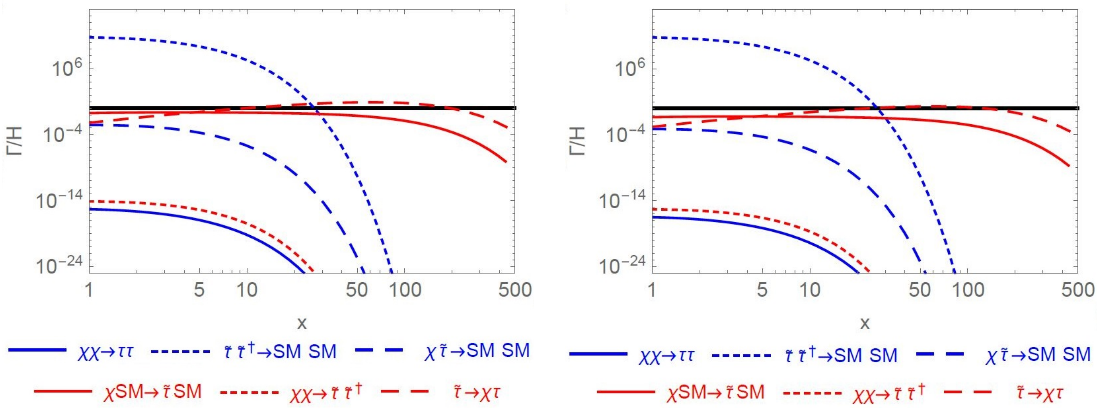

(a) $\lambda_\chi = 2 \cdot 10^{-7}$

(b) $\lambda_\chi = 10^{-7}$

Figure 2.8: Checking the efficiencies of all the co-annihilation (blue) and conversion (red) processes as a function of the temperature. Both figures are calculated with $\widetilde{\tau}$ as the co-annihilation partner and for the parameters $m_\chi = 150$ GeV and $\Delta m = 5$ GeV but for two different values of the coupling, $\lambda_\chi = 2 \cdot 10^{-7}$ (left) and $\lambda_\chi = 10^{-7}$ (right).

other unknown particles. If this is true, we can start our analysis with a negligible initial abundance. If we look at figure 2.9 which depicts the yield for small values of x for different initial conditions, we see that for $Y_\chi[1] \leq 0.1 \cdot Y_{\chi,eq}[1]$, the yield first grows and converges to a fixed value. This means that for small values of the initial yield, we do not need a exact value. Small deviations still converge. The only problem is that we can not know for sure that this assumptions is true. There are some mechanisms that might provide a respectable amount of dark matter at $x = 1$, so in the further analysis, we will try to avoid values for the coupling lower than $2 \cdot 10^{-7}$. For $\lambda_\chi > 2 \cdot 10^{-7}$, we can say that the error we make is relatively small, so we will obtain more or less the correct answer by assuming chemical equilibrium as a starting condition.

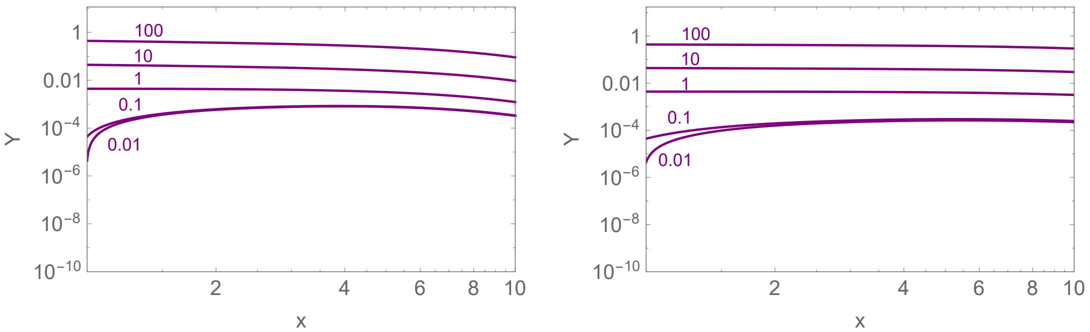

(a) $\lambda_\chi = 2 \cdot 10^{-7}$

(b) $\lambda_\chi = 10^{-7}$

Figure 2.9: Plotting the evolution of the yield for different initial conditions: $Y_\chi[1] = i \cdot Y_{\chi,eq}[1]$ with $i \in \{0.01, 0.1, 1, 10, 100\}$. It is the same plot as in figure 2.7 zoomed in for small values of x, from 1 to 10. Both figures (a) and (b) are calculated with $\widetilde{\tau}$ as the co-annihilation partner and for the parameters $m_\chi = 150$ GeV and $\Delta m = 5$ GeV but for two different values of the coupling, $\lambda_\chi = 2 \cdot 10^{-7}$ (left) and $\lambda_\chi = 10^{-7}$ (right).

Chapter 3

Relevance of conversion-driven freeze-out

An important aspect of the study of DM models is to look at how the DM is produced in the early universe. If we know this, we can also calculate how abundant the DM is today and compare it with the value obtained by the CMB, $\Omega_{DM}h^2 = 0.12$. If a model produces too much DM, we know it can not be correct and we need to implement some modifications. The same applies for an under-abundant DM component, although here, we could also consider extra contributions to the DM. However, we neglect this possibility in our analysis.

The freeze-out mechanism we introduced in section 1.3.1 is one of the most popular production mechanisms. However, the standard freeze-out mechanism can only reproduce the correct relic abundance of 0.12 for a certain range of values of the free parameters of the model under study (equation 2.4). To explore the viability of the model in other ranges of the parameters, alternative production mechanisms need to be considered, like the one we introduced in section 2.2. In this chapter, we study the difference between the standard freeze-out mechanism and the alternative conversion-driven freeze-out mechanism. We do this for the simplified model we introduced in section 2.1. First, we illustrate why the freeze-out is not able to always reproduce the correct relic abundance and how the conversion-driven freeze-out solves this issue. This is done in section 3.1. With this knowledge, we can study in which region of parameter space the standard freeze-out is not able to reproduce the correct relic DM abundance and the conversion-driven freeze-out becomes important. All this is done in section 3.2. Finally, we do a more detailed study of the lifetime of the slepton. This is particularly interesting in the context of collider searches, which we will discuss later in chapter 4.

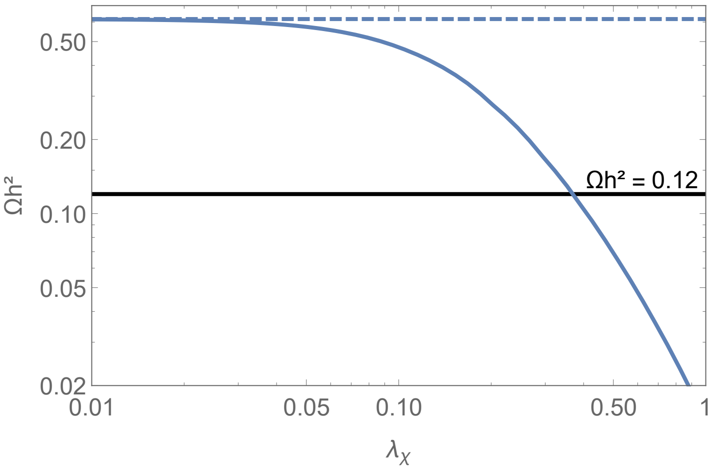

Figure 3.1: The relic abundance for different values of λ_χ with $m_\chi = 100$ GeV and $\Delta m = 5$ GeV where the co-annihilation partner is $\widetilde{\mu}$. The blue dashed curve denotes the constant value for the relic abundance in the freeze-out regime driven by $\widetilde{\tau}\widetilde{\tau}^\dagger$ annihilations. The thick black line denotes the observed relic abundances ($\Omega h^2 = 0.12$).

3.1 Finding the correct relic abundance

As we mentioned in section 2.1, the model we introduced there has three free parameters: the DM mass m_χ, the mass-splitting Δm between the DM and its co-annihilation partner and the coupling λ_χ that governs the interactions between the two partners. In the beginning of this chapter, we also said that the model has to reproduce the correct relic abundance $\Omega_{DM}h^2 = 0.12$. This puts a constraint on our model, meaning that we have only two free parameters left. We will choose m_χ and Δm freely and fix the coupling to reproduce the correct relic abundance. How this can be done is illustrated in figure 3.1. Here, we have plotted in blue the relic abundance of the DM co-annihilating with the superpartner of the muon for some fixed masses ($m_\chi = 100$ GeV and $\Delta m = 5$ GeV) while the coupling is varied on the horizontal axis. The reason for choosing $\widetilde{\mu}$ as the co-annihilation partner instead of $\widetilde{\tau}$ will become clear in the next section. The black thick line in the plot denotes the observed relic abundance $\Omega_{DM}h^2 = 0.12$. When the blue curve crosses the black one, we know that for this value of the coupling, the model reproduces the correct relic abundance. For all other values of the coupling, the model gives a wrong relic abundance and is therefore disfavoured.

Inspecting figure 3.1 more closely, we see that we are in the regime where the coupling is of the order of 10^{-1}, i.e. we are in the freeze-out regime with co-annihilations. However, it could still be that the blue line crosses the black one

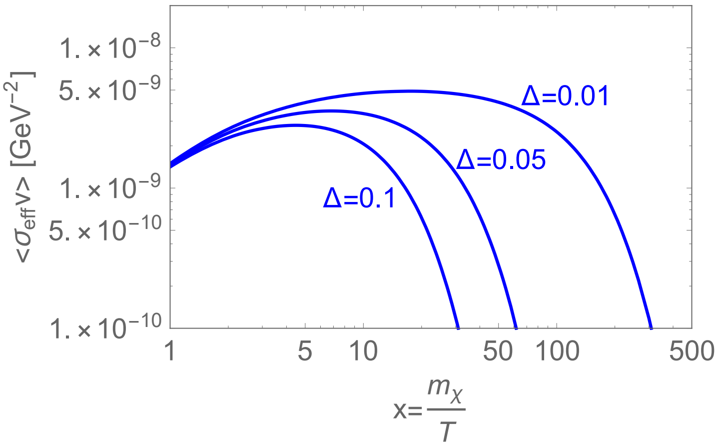

Figure 3.2: The evolution of $\langle\sigma_{eff}v\rangle$ as a function of $x = \frac{m_\chi}{T}$ for co-annihilation (equation (1.34)) of χ with $\widetilde{\mu}$ for three values of $\Delta = \frac{\Delta m}{m_\chi}$. For the calculations, the mass and coupling constant were fixed to $m_\chi = 100$ GeV and $\lambda_\chi = 10^{-5}$.

again for a smaller value of the coupling which is not shown in figure 3.1, but this is not the case. We know that for a smaller value of the coupling we enter the freeze-out regime driven by $\widetilde{\tau}\widetilde{\tau}^\dagger$ annihilations where the relic abundance does not depend on λ_χ and is therefore constant. This constant value is also shown in figure 3.1 by the dashed blue line. For a coupling of the order of 10^{-2}, the relic abundance takes this value meaning that for smaller values of λ_χ and Δm fixed, the relic abundance does not change any more. This means that in the freeze-out mechanism, the curve does not cross the 0.12 line a second time.

While applying this technique, it seems that the crossing between the blue and black curve is always for a coupling large enough to assume chemical equilibrium between the two co-annihilation partners. Indeed, for a coupling smaller than 10^{-2}, the relic abundance in figure 3.1 stays constant. By going to higher values for λ_χ, not only the annihilation of $\widetilde{\tau}$, but also the other co-annihilation processes become efficient. Therefore, the effective cross section we use to calculate the relic abundance in the standard freeze-out mechanism (equation 1.32) increases keeping the DM longer in equilibrium as we explained in section 1.3.1. This will cause a decrease of the relic abundance for larger values of the coupling so that the blue curve eventually crosses the 0.12 line. This means that as long as the dashed line denoting the final abundance for small coupling lies above the black 0.12 line at fixed Δm, the standard freeze-out mechanism is always able to reproduce the correct relic abundance. This feature can be modified by changing the mass-splitting Δm.

In figure 3.2, we see that for a smaller mass-splitting, the effective cross section

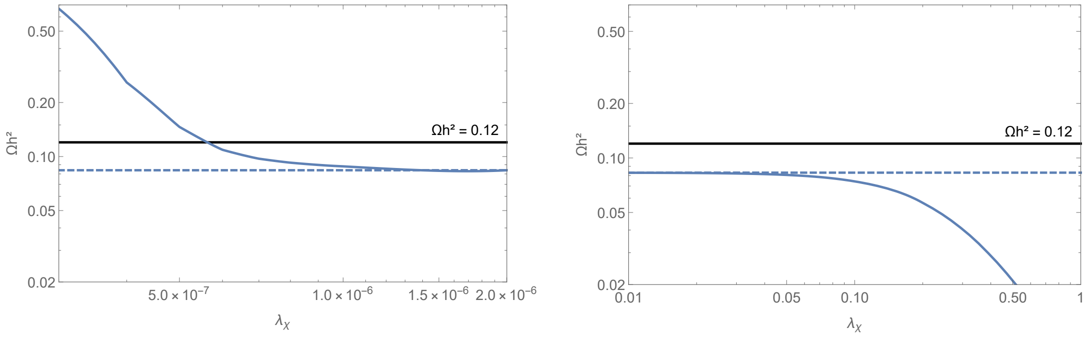

(a) (b)

Figure 3.3: The relic abundance for different values of λ_χ with $m_\chi = 100\ GeV$ and $\Delta m = 1\ GeV$ where the co-annihilation partner is $\widetilde{\mu}$. The blue dashed curve denotes the constant value for the relic abundance calculated in the freeze-out regime driven by $\widetilde{\tau}\widetilde{\tau}^\dagger$ annihilations. The thick black line denotes the observed relic abundances ($\Omega_{DM}h^2 = 0.12$). On the left, we are in the conversion-driven freeze-out regime. The right picture denotes the standard freeze-out regime. We see that they both converge to the intermediate freeze-out regime driven by $\widetilde{\tau}\widetilde{\tau}^\dagger$ annihilation.

is larger and stays large for higher values of x. Therefore, χ remains longer in equilibrium resulting in a smaller abundance. This means that for small mass differences, it could be that the relic abundance in the freeze-out regime driven by $\widetilde{\tau}\widetilde{\tau}^\dagger$ annihilations is smaller than 0.12. An example of such a case can be found in figure 3.3b. In this regime, the standard co-annihilation mechanism cannot give the correct relic abundance for any value of λ_χ because lowering the coupling (even to extremely small values) does not change the final abundance. We know however that for these very small values of λ_χ (of the order of 10^{-7}), the assumption of chemical equilibrium between $\widetilde{\tau}$ and χ breaks down because the conversion processes become inefficient. This is when the conversion-driven freeze-out mechanism becomes relevant. In chapter 2, we learned how to calculate the relic abundance in this case. Figure 3.3a illustrates what happens in this regime. The calculated final abundance starts to grow again if we move to smaller couplings.

With the knowledge we gained in chapter 2, we are able to explain this behaviour for very small values of the coupling. We know that if the conversion processes are efficient, i.e. for couplings larger than 10^{-6}, χ is in equilibrium with its co-annihilation partner which at his turn is in equilibrium with the SM particles through the annihilation process $\widetilde{\tau}\widetilde{\tau}^\dagger \leftrightarrow SM\ SM$. Therefore, the DM abundance tracks its equilibrium value. The equilibrium abundance is decreasing, so the DM abundance too gets dragged down. However, for smaller values of λ_χ, the conversion rates eventually becomes smaller than the Hubble rate. Indeed, as seen in figure 2.8, initially, the conversion processes are inefficient and the DM yield is not influenced and stays constant. At a certain moment, the decay rate becomes larger than the Hubble rate. At that point in time, conversion is efficient and tries to bring the DM abundance to its equilibrium value. Because this value is already quite low compared to its initial value, the DM yield is dragged down. After a while, the decay ceases to be efficient and the DM yield stays constant again. The timespan where $\Gamma > H$ is not long enough to bring χ completely in equilibrium. The shorter the period, the less the abundance gets dragged down. This means that we obtain a larger relic abundance for smaller values of the coupling because the timespan where $\Gamma > H$ is shorter in this case. As a consequence of the rising abundance, the curve in figure 3.3a eventually crosses the black 0.12 line and we are able reproduce the correct relic abundance, even when the standard freeze-out mechanism fails to give a solution. The main difference is that the coupling constant λ_χ is very small compared to the solutions where chemical equilibrium is assumed.

3.2 Looking for the viable parameter region

The next step in our analysis is to really dive into parameter space and look where the standard freeze-out mechanism fails to reproduce the observed relic abundance. This is exactly the region where we need the conversion-driven freeze-out to produce the DM meaning that in this region, λ_χ is rather small, of the order of 10^{-7}. This is an interesting region because such a small coupling makes the lifetime of the slepton macroscopic. It is particularly interesting because most collider searches mainly focus on prompt (immediate) decay while still a lot can be done for displaced decay. We will focus more on this in the next section. First we need to find out how we can retrieve the region where freeze-out fails to reproduce the correct DM abundance. We saw in the previous section that this happens when the relic abundance predicted by freeze-out is smaller than 0.12 in the freeze-out regime without co-annihilations, i.e. for values of λ_χ smaller than 10^{-2}. To find the desired region in parameter space, it is sufficient to calculate the relic abundance with the standard freeze-out mechanism with a sufficiently small coupling ($\lambda_\chi \sim 10^{-5}$) and see where the solution is smaller than 0.12. Indeed, in such region, the conversion-driven freeze-out mechanism can lead to an increase of the DM relic abundance if we set the coupling to a smaller value, of the order of 10^{-7}. The results for the three flavours of sleptons separately can be found in figure 3.4. To obtain these curves, the relic abundance was calculated with the standard freeze-out mechanism presented in section 1.3 with $\lambda_\chi = 10^{-5}$ for a certain amount of points on a grid. More specific, the grid was ranging for m_χ from 50 to 200 GeV, with a 25 GeV interval between points, and for Δm ranging form 0.1 to 2.1 with an interval of 0.2 and one additional point $\Delta m = 0.01$. To obtain the position of the 0.12 line in the $m_\chi - \Delta m$ plane, we interpolated these results.

Let us first have a look at the most heavy lepton of the three, the tau. The calculated result for the 0.12 curve is denoted by the green curve in figure 3.3a. The DM mass range where we can have conversion-driven freeze-out is not very large, we can only go up to masses around 180 GeV. To have a mass of about 150 GeV, a mass splitting less than 1 GeV is needed. However, if $\Delta m < m_\tau = 1.777$ GeV, the decay process $\widetilde{\tau} \to \chi\tau$ is kinematically forbidden and three or four body decays like the ones in figure 3.5 become dominant. These processes are suppressed by the off-shell intermediate particles and the multi-body phase space which makes the decay rate small. The decay of the stau is the most important conversion process that keeps χ coupled to his co-annihilation partner, but if it is too small, this chemical contact is broken. Therefore, the freeze-in mechanism would determine the relic abundance in the regime where $\Delta m < m_\tau$. Another consequence is that the results in figure 3.4 are not correct in this regime because we assume chemical equilibrium. We hence have covered this portion of parameter space in red and we will not further study it. More studies on this region can be found in [62]. We want to discuss where the conversion driven freeze-out mechanism can provide the correct relic abundance and therefore, we shall not consider this region. This restricts our possibilities significantly. Now we can go only to masses up to 80 GeV for the DM. This is not very high taking into account the mass limits on the stau [55]. These limits are mainly obtained by the Large Electron-Positron collider (LEP), the predecessor of the LHC at CERN. In the analysis of the LEP data, different assumptions were made which probe slightly different limits. Most limits for the three flavours lie between 80 and 100 GeV. We take the one that depends the least on the underlying model. For the stau, the limit is 90 GeV [56], for the smuon 88 GeV [57] and for the selectron 73 GeV [58]. The limits are denoted by the grey regions in figure 3.4. It is now clear that in the stau case, nothing of our available green parameter space is left. This basically means that conversion-driven freeze-out with $\widetilde{\tau}$ as co-annihilation partner is not able to reproduce the correct relic abundance in the available parameter space. Thus, we can already exclude the stau-Majorana DM model as a working example for conversion-driven freeze-out.

There are still two other possible leptophilic models, with the smuon and selectron as the dark sector partner for the DM. The green region in figure 3.4 where conversion-driven freeze-out is the DM production mechanism that reproduces the correct relic abundance is about the same for all three possible co-annihilation partners. The main difference is where the two body decay becomes kinematically forbidden. Due to the smaller masses for the electron ($m_e = 511$ keV) and

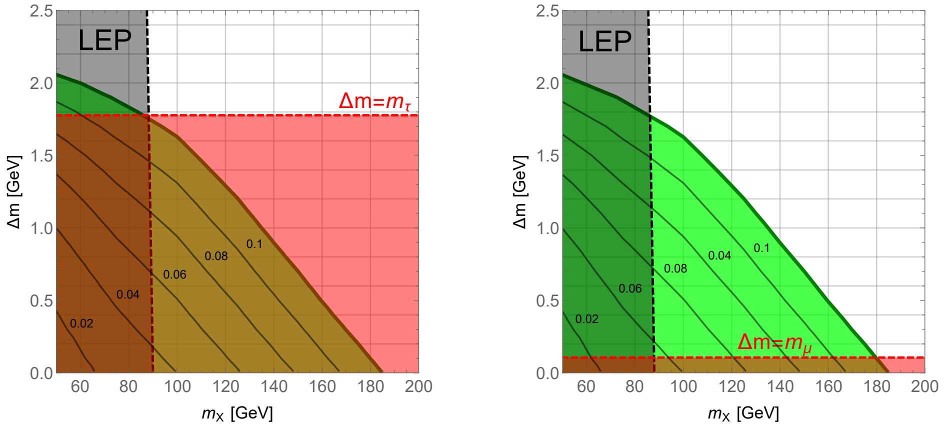

(a) $\widetilde{\tau}$ co-annihilation

(b) $\widetilde{\mu}$ co-annihilation

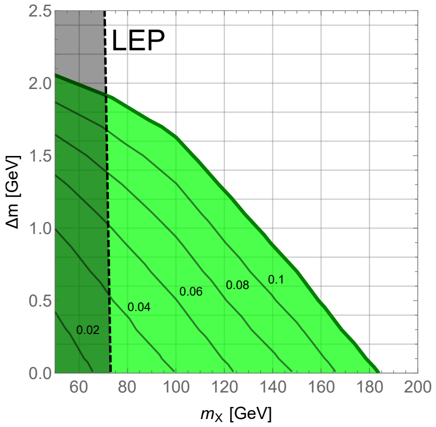

(c) $\widetilde{e}$ co-annihilation

Figure 3.4: Some contours of the relic abundance in the standard freeze-out paradigm when the annihilation of the $\widetilde{l}$ is driving the abundance, i.e. when $\Omega_{DM}h^2$ is independent of λ_χ. The thick green curve denotes an abundance of 0.12. This is the border between the regions where chemical equilibrium can be assumed (above) and where it does not hold (below). This last region is coloured in green because it is the region where conversion-driven freeze-out is able to reproduce the correct relic abundance. The analysis has been done for each of the three sleptons coupling to the DM. The red line denotes when the mass splitting equals the mass of the corresponding lepton. Below this line, our results can not be trusted. Therefore, this region is coloured in red. In black, the mass limits of the sleptons coming from LEP are displayed. For the stau, the limit is 90 GeV [56], for the smuon 88 GeV [57] and for the selectron 73 GeV [58]

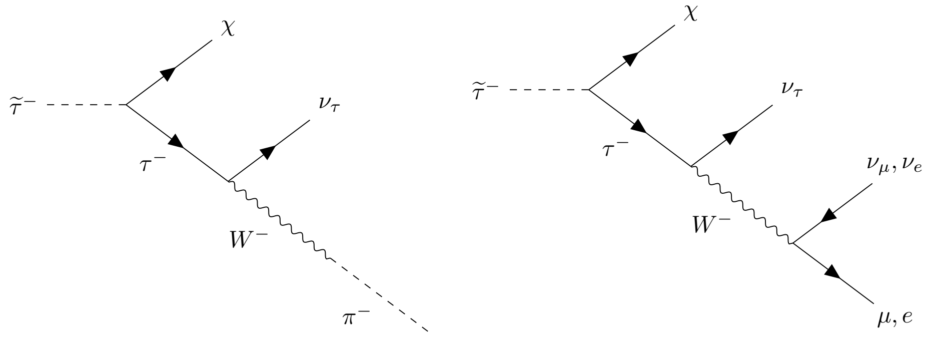

(a) (b)

Figure 3.5: Feynman diagrams of the three (left) and four (right) body decay of $\widetilde{\tau}$ that would have to be taken into account when $\Delta m < m_\tau$.

muon ($m_\mu = 106$ MeV), the forbidden region in red becomes smaller and a region where the conversion-driven solution can reproduce the correct relic DM abundance opens. If the smuon is the co-annihilation partner, the DM mass can go up to 180 GeV. For the selectron, it can go even a bit above this value. In this case, the mass limits for LEP do not constrain all of our parameter space. This leaves us enough room for conversion-driven freeze-out to be a possible production mechanism for dark matter with $\widetilde{\mu}$ or $\widetilde{e}$ as the co-annihilation partner.

3.3 Lifetime of the sleptons

In the previous sections, we have determined in which region of parameter space the standard freeze-out mechanism is valid and when we have to use conversion-driven freeze-out. We also studied which values the coupling constant typically takes in these two possible cases. In figure 3.1 and 3.3, we see that for the freeze-out, we have a coupling somewhere between 10^{-2} and 1 while for the conversion-driven freeze-out we need a rather small coupling, of the order of 10^{-7}. This has important consequences for the lifetime of the sleptons because they decay via the process $\widetilde{l} \to \chi l$. The decay rate depends on the square of the coupling constant,

$$\Gamma_{\widetilde{l}} = \lambda_\chi^2 \frac{(m_{\widetilde{l}}^2 - m_l^2 - m_\chi^2)\sqrt{\left[m_{\widetilde{l}}^2 - (m_\chi - m_l)^2\right]\left[m_{\widetilde{l}}^2 - (m_\chi + m_l)^2\right]}}{16\pi m_{\widetilde{l}}^3}, \tag{3.1}$$

$$\approx \frac{\lambda_\chi^2 \Delta m^2}{4\pi m_\chi}\left[1 - \frac{2\Delta m}{m_\chi} + \dots\right], \tag{3.2}$$

where in the last line, we neglected the lepton mass ($m_l \ll m_\chi, m_{\widetilde{l}}$) and expanded for small Δm. We see that $\Gamma_{\widetilde{l}} \propto \lambda_\chi^2$ meaning that for a small values of the coupling,

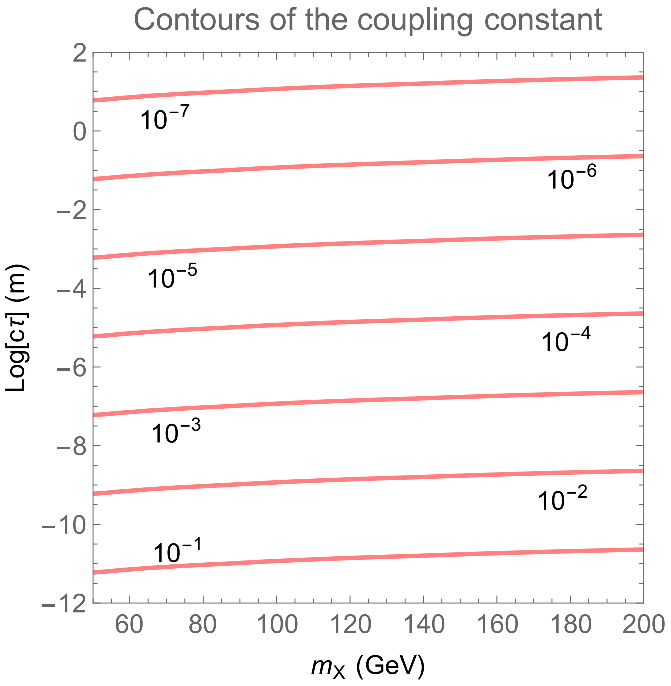

Figure 3.6: Contours of the coupling constant λ_χ for different values of the DM mass m_χ and the smuon lifetime $c\tau$. A fixed mass splitting $\Delta m = 1$ GeV is assumed during the calculations.

the rate is small too. A small rate implies a long lifetime because $\tau_{\tilde{l}} = \frac{1}{\Gamma_{\tilde{l}}}$ and therefore also a long decay length $c\tau_{\tilde{l}}$. In figure 3.6, we can see the dependence of the decay length on the coupling when the slepton is a smuon and a fixed mass splitting of $\Delta m = 1$ GeV is assumed. The stau and selectron have a very similar dependence because the decay rate (equation (3.1)) is the same for the three flavours, only the mass of the lepton is different.

The lifetime of a particle is an interesting property in the context of collider searches. If the lifetime is very short, particles decay prompt, i.e. before they reach the tracker. Therefore, only the decay products leave a signal inside the detector. On the other hand, if the lifetime is very long, the particles might fully traverse the detector. Depending on this, different signatures are to be looked for in the data coming from collider experiments. We will discuss this in more detail in chapter 4. Because it is such an important property, it is useful to study the decay of the sleptons in the model we presented in section 2.1. We look for which values of the decay length conversion-driven freeze-out reproduces the correct relic abundance. In the previous section, we saw that conversion-driven freeze-out with the $\tilde{\tau}$ as the co-annihilation partner only reproduces the observed abundance in a region that has already been excluded by LEP. Therefore, we do not consider the

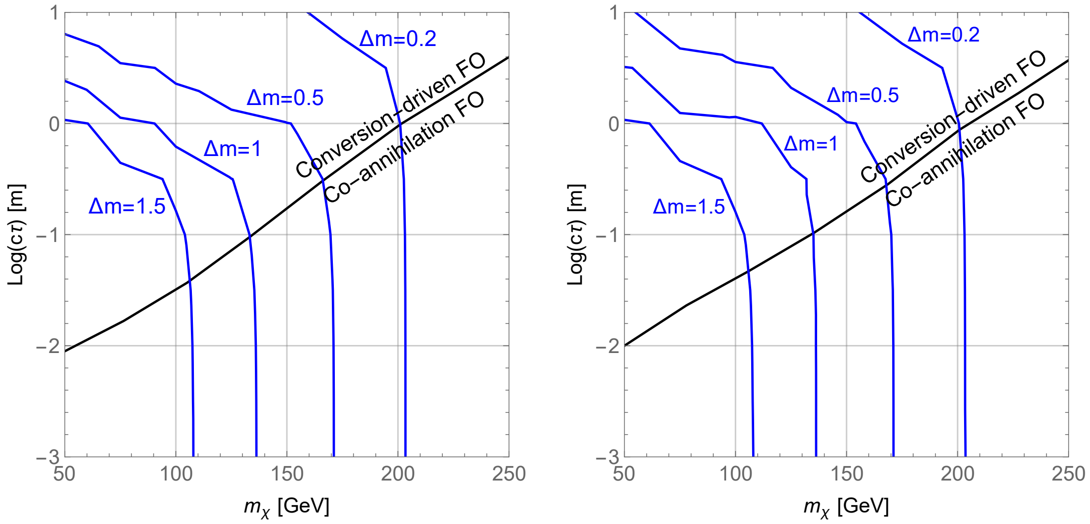

(a) $\widetilde{\mu}$ co-annihilation

(b) $\widetilde{e}$ co-annihilation

Figure 3.7: Lines where we are able to reproduce the correct relic abundance in the $c\tau - m_\chi$ plane for different values of the mass-splitting $\Delta m \in \{0.2, 0.5, 1, 1.5\}$ GeV. The left one contains the results when χ couples to the smuon, on the right we find the case for the selectron. The black line denotes the approximate border where the co-annihilations (standard) Freeze-Out (FO) or the conversion-driven freeze-out mechanism reproduce the correct DM abundance that is shown as a guide for the eye.

case of the staus here, only the smuons and selectrons.

In figure 3.7, it is shown for which values of the decay length $c\tau$, the DM mass m_χ and mass-splitting Δm it is possible to obtain the correct relic abundance with the conversion-driven freeze-out mechanism. This plot has been obtained in a similar way as the ones in figure 3.4. We calculated the relic abundance for some grid points, m_χ ranging from 50 GeV to 250 GeV with an interval of 25 GeV and $c\tau$ (m) ranging on a log scale from -3 to 1 with an interval of 0.5, and interpolated those results.

The shape of the curves in figure 3.7 can be explained by the behaviour we saw in the different regimes in section 2.3.2 and the things we learned in the previous sections of this chapter. In section 3.1, we investigated how the relic abundance depends on λ_χ. Because the decay length is strongly correlated to the coupling constant as we saw in equation (3.1) and figure 3.6, the behaviour is very similar. For instance, for large decay lengths, the coupling is small enough such that conversion-driven freeze-out plays a role. In this production scenario, the relic abundance changes significantly if we change λ_χ a little bit. If we go to smaller values of $c\tau$ around 10 cm (depending on the mass splitting), we enter the freeze-out regime driven by $\widetilde{\tau}\widetilde{\tau}^{\dagger}$ annihilations. In this regime, λ_χ plays no role and therefore, the final abundance will not change for different values of $c\tau$. Thus, the curve denoting a fixed abundance of 0.12 will become vertical. This means that for the value of the mass where the vertical line is located for a fixed Δm, the decay length is not fixed by the constraint that the relic abundance should be 0.12. A whole range of possibilities is open, and there is no reason why we can prefer one value over another. This is a strange feature, but to obtain this, the mass and mass-splitting must be perfectly tuned. The border between the conversion-driven freeze-out regime (where the curve bends) and the standard freeze-out regime (where the curve is vertical) is approximately shown with a black solid line in figure 3.7 as a guide for the eye. If we would decrease the coupling (or equivalent, the decay length) even further, the straight line would start to bend again because the coupling is large enough such that the co-annihilations processes $\chi\chi \leftrightarrow SM\ SM$ and $\chi\widetilde{l} \leftrightarrow SM\ SM$ start to play a role. However, the coupling constant in this region is such that the slepton has a very short lifetime. This effect is not shown in figure 3.7 because we are interested in long-lived sleptons with a decay length of a few millimetres to a couple metres. The reason why we are only interested in this type of sleptons will become clear in chapter 4.

The fact that the relic abundance curve becomes vertical in figure 3.7 has some very important consequences for our model. The value for the DM mass where this happens is the maximal value we can achieve for a fixed value of Δm in the conversion-driven freeze-out mechanism. It is possible to reproduce the correct relic abundance for every value of the DM mass lower than this maximal value (and above the LEP constraints), but the lifetime is larger, as we can deduce from figure 3.7. We can not go to higher masses, unless we go to the standard freeze-out regime with co-annihilations ($\lambda_\chi > 10^{-2}$), which we do not consider here. If we compare the curves for different values of the mass-splitting, we see that if we lower Δm, we can achieve higher masses. This is something we already predicted from the results in section 3.2.

From the knowledge we obtained in section 3.2, we can also predict something else. By studying figure 3.4, we can deduce at which masses we enter the standard freeze-out regime for a fixed value of Δm. This border is denoted in figure 3.4 by the thick green curve. For instance for the case of the smuons, we see that for a mass splitting of 1 GeV, this border is at about 135 GeV. In figure 3.6a, we can find the vertical part of the line representing a mass splitting of 1 GeV at about the same mass of 135 GeV[1].

---

[1] If we reduce the mass-splitting, we observe a small discrepancy (about 15%) between figures 3.3b and 3.6a. This is because for figure 3.3b, we used the approximated equations for the standard freeze-out mechanism we introduced in section 1.3.3 while in figure 3.6a, we used the complete set of coupled Boltzmann equations from section 2.2 to obtain the results for the

Another important effect is that for smaller values of the mass-splitting, the curve denoting the correct relic abundance starts to bend at larger lifetimes. This makes that the conversion-driven freeze-out regime starts at larger values of the lifetime if we decrease the value of Δm. Therefore, when the DM has a fixed mass, the lifetime becomes longer if we decrease the mass-splitting. This is something we would expect because for a smaller mass-splitting, the conversion processes are larger making that the co-annihilation partners stay in equilibrium for smaller values of the coupling. For conversion-driven freeze-out to become important, this contact has to be broken.

The difference between the cases where a different slepton flavour couples to the DM is the corresponding lepton that plays a role. The mass of the lepton is the only constant in our model that has a different value in the three different cases. In the previous section, we saw that the differences between the relic abundance contours in the three cases were minor. Also now, when we are using the conversion-driven freeze-out mechanism, the results of the $\widetilde{\mu}$ and $\widetilde{e}$ in figure 3.7 are very similar. The value of the lepton mass does not impact the results because it is dominated by the slepton and DM mass which are much larger. The only importance is that it restricts the mass-splitting we can use, because when $\Delta m < m_l$, three and four body decay start to play a role changing the decay rate (see section 3.2). Thus, for the case of the selectrons, we can use a smaller values for mass-splitting.

In the next chapter, we discuss how collider searches can probe the parameter space of the model in the conversion-driven freeze-out regime. This is done with the results in figure 3.7 which have been thoroughly discussed here. This provides a connection between the simplified DM model, the DM abundance and the corresponding collider signatures.

---

conversion-driven freeze-out mechanism.

Chapter 4

Collider constraints

The largest particle collider in the world today is located under the Swiss-French border. At CERN, the Large Hadron Collider (LHC) is a circular collider that has a circumference of 27 kilometres and currently collides protons with each other at energies up to 13 TeV. LHC can already account for some very important discoveries. Not only did it very accurate measurements of various fundamental parameters, it is also responsible for the ground-breaking discovery of the Brout-Englert-Higgs boson [63, 64]. With this detection in 2012, the standard model of particle physics was fully confirmed and the search for new physics started. Theorists expected to see new particles appearing at electroweak scales, but unfortunately, this has not happened so far. The popular extension of the standard model called Weak-scale supersymmetry, with the neutralino as a very popular DM candidate, is therefore subjected to more and more stringent constraints as time passes. The absence of clear signals of new physics can mean three thing. First, it might be that we are looking for a type of particle that does not exist and that something else like PBHs make up DM. It could also be that they are just around the corner such that they will be discovered in the near future. A third option is that they are somehow hidden for the existing searches. The majority of the DM LHC searches are focussing on prompt signatures, meaning that only very unstable particles which decay immediately after they are produced can be seen in these searches. This means that the dark matter would be only visible via missing energy as we already explained in section 1.4. Because such signals are not observed yet, a variety of mechanisms have been devised that could hide new physics from collider searches. New particles with macroscopic decay lengths for instance can escape the searches that focus on prompt decays. In theories like Gauge-Mediated SUSY Breaking [65] (GMSB), particles with macroscopic decay lengths arise. Also in the simplified model we introduced in chapter 2, this is possible because the value for the coupling constant λ_χ is not fixed. If we take this to be small, the decay rate for $\widetilde{l} \to l\ \chi$ is small, making the sleptons long-lived.

To understand what kind of exotic signatures can occur at colliders, we first need to know a bit about how these detectors work. Therefore, we start this chapter by going over the main detection mechanisms used in these detectors. Once we did this, we can go on and think about the different signatures that can be related to long-lived sleptons. There are already some searches that have been done at LHC, so to end this chapter, we look at how these searches constrain our simplified model.

4.1 Collider detectors

At accelerators, particles are boosted to very high energies before they are made to collide. These collisions happen at specific places where detectors are build around the pipe in which the collision happens. The detectors are build in such a way that they could measure properties like the speed, mass and charge of the particles that are created in the collision. To do this, the detector is made out of layers of sub-detectors each designed to look for particular properties or specific types of particles. First of all, the produced particles travel through a tracking device. This reveals the paths of electrically charged particles as they pass through and interact with suitable substances. The tracker records tiny electrical signals that are triggered by these interactions which are later used by a computer program to reconstruct the track. Normally, the particles would just travel in straight lines but in the presence of a magnetic field, their paths become curved. Therefore, electromagnets are placed around particle detectors to exploit this effect. From the curvature of the particles track, it is possible to calculate its momentum: particles with a high momentum travel almost in straight paths while ones with very low momentum move forward in tight spirals. In this way, the momentum of all particles can be found. However, there is one exception. The muon interacts very little with matter and can therefore travel through meters of dense material before being stopped. For this reason, tracking devices specially made to detect muons usually make up the outermost layer of the detector as can be seen in figure 4.1 for the CMS detector at LHC.

The second layer of the detector is made out of the calorimeters. These devices measures the energy a particle loses as it passes through. They are usually thick enough to stop or absorb most of the particles coming from a collision and in this way, it is possible to find the energy it had at the time it was produced. There are two types of calorimeters. The electromagnetic calorimeter measure the energy of the electrons and photons as they interact with the electrically charged particles in matter. Besides that, there is also the hadronic one which does effectively the same but for hadrons when they interact with the atomic nuclei.

If a particle has passed through the tracker and calorimeters, there are two

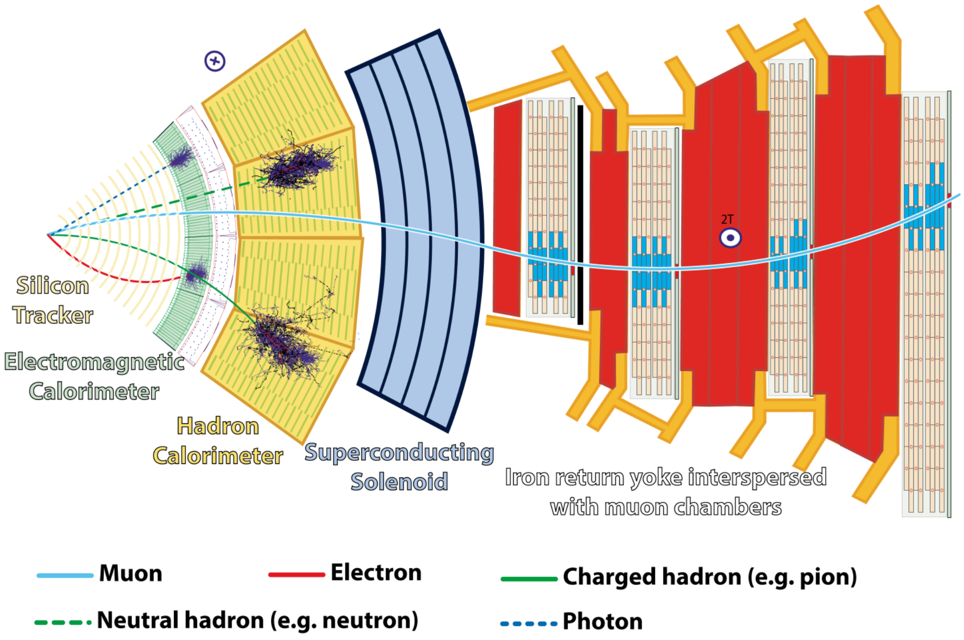

Figure 4.1: A slice of the CMS detector and where all different particles are detected [66].

other methods of narrowing down its identity. They both rely on the Cherenkov radiation a particle emits when it travels faster than light does through a given medium. This radiation is emitted under a certain angle which depends on the velocity of the particle. Together with the measured momentum, it is possible to calculate the mass and therefore determine the identity of the particle. Also, when charged particles cross the boundary between two electrical insulators with different resistance, it emits radiation. The phenomena is related to the energy of the particle and can therefore be used by physicists to distinguish the different types of particles.

Collecting all these clues from the different part of the detector, it is possible to build up a snapshot of what was in the detector when the collision happened. When some exotic things happen that cannot occur in the standard model, they are included in this snapshot and physicist can start interpreting this data [67].

4.2 Collider searches

There are already several existing searches for long-lived particles at the LHC. One of the motivations for these searches in the context of SUSY appear in models of GMSB, where the long-lived $\tilde{\tau}_R$ is the Next to Lightest SuperParticle (NLSP) with

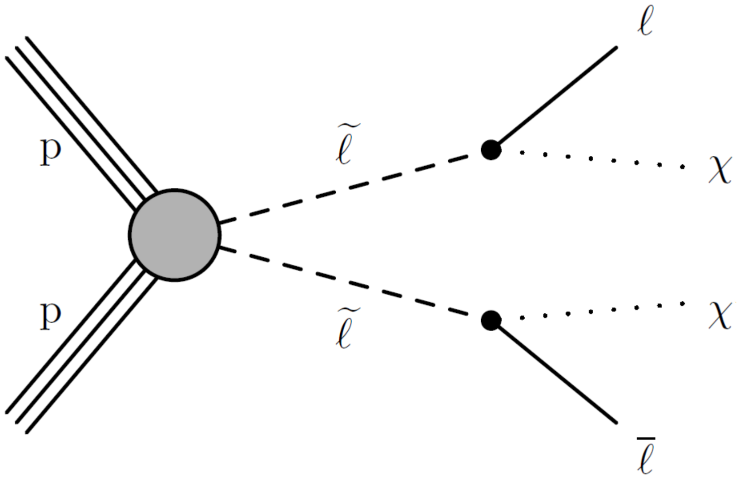

Figure 4.2: Diagram for slepton pair production at LHC with direct decay into a leptons and DM which is denoted by a dotted line because it can not be directly detected [68].

the gravitino $\widetilde{G}$ as the Lightest SuperParticle (LSP). Searches targeting the stau can be relevant for the model studied in this thesis. Depending on the lifetime of the stau, there are mainly three types of signatures that can occur in the detector. We quickly review them here in the context of the simplified model introduced in chapter 2 where the long-lived particles are the sleptons.

Heavy stable charged particles

In the detectors at LHC, the tracking devices are able to reconstruct the paths of particles traversing the detector. Only charged particles can be detected with these trackers and therefore, the neutral DM particle can not be seen in the detector. However, other dark sector particles like the sleptons in our model can give a clear signal. We have seen in chapter 2 that the sleptons can decay to dark matter via $\widetilde{l} \rightarrow \chi l$. This process depends on the coupling constant λ_χ which can take arbitrary values. Therefore, if λ_χ is very small, the lifetime of the sleptons can become quite long ($c\tau > 1$ m) such that they can traverse the tracker completely. When this is the case, we call the slepton "detector-stable", meaning its decay length is larger than the radius of the detector. In this regime, the Heavy Stable Charged Particles (HSCP) searches performed at the CMS detector [69] can become very useful not to put constraints directly on DM but on the sleptons. Limits on the mass of detector-stable sleptons are already available. Of course, if we specify the mass splitting Δm, the HSCP searches can give constraints on DM too, but this is model dependent.

Kinked and disappearing tracks

The coupling constant λ_χ is not fixed in our model, so it can still be that the sleptons are not detector-stable. For instance, if the decay length of the sleptons is of the order of 50 cm, they decay inside the tracking device and this signal is not included in the HSCP searches. They only look for events that leave a complete track in the detector. Nevertheless, there are some other strategies for finding particles with a macroscopic decay length. We know that the sleptons decay into their corresponding lepton and the DM. Because the DM is neutral, it can not be detected in the tracker. However, the other daughter particle, the lepton, can leave a track. If the sleptons decay while traversing the tracker, its track suddenly stops, but a new one coming from the lepton starts where the slepton track has ended. Thus, there is a complete track going through the tracker, but the lepton is emitted under an angle and therefore, the track shows a kink where the slepton has decayed. These types of tracks were investigated at LEP [70], but at LHC, it is more difficult. Due to the busier environment, the track associated with the daughter lepton is typically not reconstructed or may not be associated with the parent slepton track. Therefore, triggering on these kinked tracks is nearly impossible. Since the lepton track is often not detected and the DM leaves no track at all, the slepton track just stops in the middle of the tracker. These tracks are named disappearing tracks and have already been investigated at LHC by both CMS [71] and ATLAS [72]. These searches give limits on $\widetilde{l}$ if the decay length is of the order of 50 cm.

Opposite-sign displaced leptons

A third thing that can happen is that the decay is not prompt, but still happens before the slepton enters the tracker. Then, the daughter leptons leave a complete track inside the detector, while the DM just flies through. Now we can ask ourself how we can distinguish these leptons coming from the decay of the sleptons from the other ones produced in the collision. The difference is that the daughter leptons does not originate from the collision vertex but rather from the place where the slepton decays. This can be a couple millimetres up to some centimeters away from the primary vertex. We refer to this as a displaced vertex.

In figure 4.2, we can see how two opposite-sign leptons can be created from the proton-proton collision together with two DM particles. Unfortunately, there are not many searches performed for opposite-sign displaced leptons yet. At LHC, the CMS displaced $e\mu$ search [73] is currently the only one existing. This search is mostly concentrating on a stop that can decay into a bottom quark and a lepton. In a similar way as two opposite sign sleptons are produced in figure 4.2, two opposite sign stops can be produced from the collision and decay into a pair of opposite sign leptons. This process has been studied by looking at a displaced $e\mu$ pair. The analysis was recasted to give limits on the decay of sleptons which produce a pair of opposite sign same flavour leptons [74].

4.3 Constraints from collider searches

In the previous section, we explained how researchers already tried to observe long-lived sleptons at the LHC depending on the lifetime. However, no clear signal has been observed yet and this sets bounds on the long-lived sleptons (or long-lived particles in general). Not all these bounds are very strong because there has not been much interest in these kind of signals for a long time. This is because these searches are difficult to perform, especially the disappearing tracks and displaced lepton searches. Therefore, the limits coming from these searches are not as stringent as the limits coming from prompt or HSCP searches. The long-lived slepton limits are shown in figure 4.3. We also want to see how these searches constrain the model we introduced in chapter 2. Therefore, we add the curves which depict when the conversion-driven freeze-out mechanism reproduces the correct relic abundance for different values of the mass-splitting Δm. These curves were already presented in figure 3.7 but are here denoted in the $m_{\tilde{l}} - c\tau$ plane instead of the $m_\chi - c\tau$ plane. This change is made because all the limits are on the slepton mass since this is the particle that can be observed at colliders, contrary to DM. However, the change is not very radical because we assume a small splitting between the slepton and DM mass. The excluded regions by OPAL at LEP [70] are also denoted in this figure by the grey area.

In figure 4.3, the 95% exclusion limits of the HSCP search are depicted by the red, solid curve, together with a 25% uncertainty band to the modelling of this search. Everything above is excluded. As we can see, these limits for long-lived sleptons are only important for a large lifetime, i.e. when $c\tau$ is of the order of a meter. This is because only then, the particles fully traverse the tracker and are included in the search. This means that there are no limits set on particles that does not pass completely through the tracker by this search. The constraints coming from the HSCP searches are very important because they are present in a large mass range (which is not the case for the other two types of searches). We see that for larger masses ($m_\chi > 200$ GeV), the bound becomes less strong. However, in our model, we are more interested in masses smaller than 200 GeV. For this mass range, particles with a decay length longer than approximately 3 meter can be excluded with a high probability.

The second kind of searches that study particles with macroscopic decay lengths are disappearing track searches at for instance CMS and ATLAS. These searches focus on tracks that suddenly stop in the detector indicating that the particle

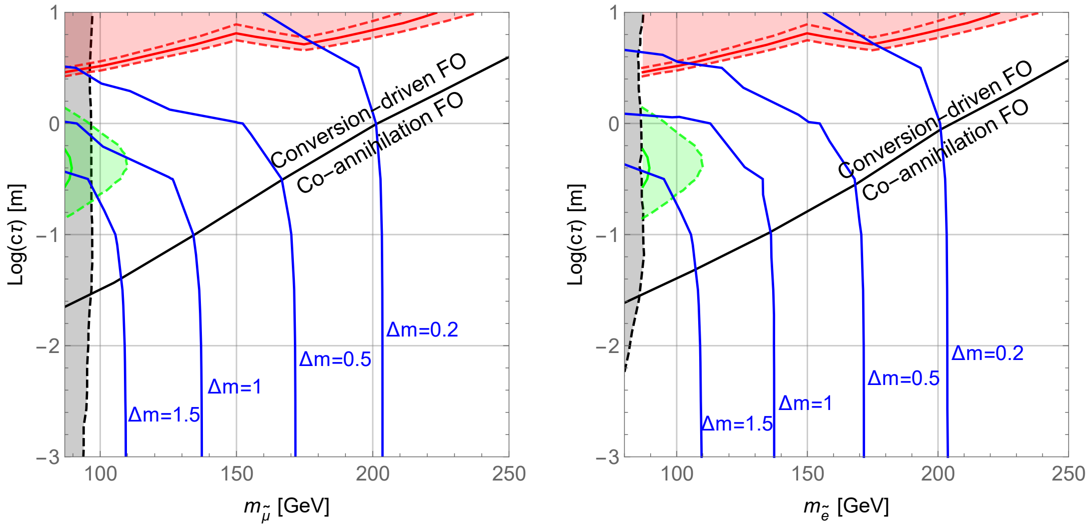

(a) $\widetilde{\mu}$ co-annihilation

(b) $\widetilde{e}$ co-annihilation

Figure 4.3: Lines where we are able to reproduce the correct relic abundance in the $c\tau - m_{\tilde{l}}$ plane for different values of the mass-splitting Δm. The left one contains the results when χ couples to the smuon, on the right we find the case for the selectron. The black line denotes the approximate border where the co-annihilations (standard) Freeze-Out (FO) or the conversion-driven freeze-out mechanism reproduce the correct DM abundance that is shown as a guide for the eye. Together with this, constraints from various searches at LEP and LHC are shown. The red solid line is the 95% exclusion limit coming from the CMS heavy stable charged particle search [69]. The band denoted by the red dashed lines represents a 25% uncertainty to the modelling of this search. The 95% exclusion limit from the disappearing track searches performed at CMS [71] and ATLAS [72] are denoted in green with a 50% modelling uncertainty band (green dashed line). Only the stronger of the two is shown. The grey area is the region excluded by OPAL at LEP [70]. The bounds from the recasting [74] of the CMS displaced $e\mu$ search [73] falls well below the OPAL bound and is therefore not show.

responsible for this track has decayed. Therefore only particles which have a lifetime long enough to reach the tracker but not that long such that they traverse it completely are constrained by these searches. The bounds coming from the disappearing track searches performed by CMS and ATLAS are depicted in green in figure 4.3. Here, the strongest bound of the two is shown (for a comparison, see [74]). Again, an modelling uncertainty band is added, this time of 50%. This is primarily because of additional uncertainty introduced by the decay product originating from the displaced secondary slepton vertex. The excluded region for the disappearing track searches is way smaller than the HSCP search. The limits are most stringent for $c\tau \approx 50$ cm, but even the strongest bound only restricts masses up to about 110 GeV which is only slightly above the bounds set by LEP. This mean that models with a coupling constant such that the lifetime of the sleptons is of this order are not constrained very strongly.

The third option we discussed in the previous section is the one of displaced leptons. Here, we look at leptons that leave a complete track but are produced a few millimetres to a couple centimetres away from the collision point. This can indicate the decay of a slepton that is produced in the collision and decays after a few centimetres. Therefore, the constraints coming from these searches are important only for particles with a decay length of this order. However, not much data has already been collected for these searches. This makes that the constraints are not very stringent, they fall well below the LEP bound and are therefore not shown in figure 4.3.

If we consider all limits together, we can see in general where our model is already constrained. In section 3.3, we noticed that in the conversion-driven freeze-out regime a smaller mass-splitting yields a longer lifetime. The strongest bounds are due to the HSCP searches, which constrain the sleptons with a long lifetime ($c\tau > 3$ m for $m_\chi \approx 100$ GeV). For instance, if we look at the curve representing the case where $\Delta m = 0.2$ GeV the conversion-driven freeze-out starts to become important when the decay length is about 1 m for both the $\widetilde{\mu}$ and $\widetilde{e}$ case. The bounds from the HSCP searches already become important around for $c\tau \approx 3$ m. If we then look at how this restricts the slepton mass, we see that for a small mass-splitting, already a large mass range is excluded. For $\Delta m = 0.2$ GeV, only slepton masses between 175 and a approximately 200 GeV are allowed for both slepton cases. If we do the same analysis for a larger mass splitting, we see that the HSCP constraints play a less important role here because we obtain smaller lifetimes for the sleptons. Therefore, a larger DM mass range opens where we can reproduce the correct relic abundance with the conversion-driven freeze-out mechanism. For instance in the smuon case, for a mass-splitting of 0.5 GeV, masses ranging from about 100 GeV to 170 Gev are allowed.

The larger the value of Δm, the less the bounds from HSCP searches constrain the model. But assuming a larger mass-splitting has some other consequences too. In section 3.3, we explained that this reduced the maximal allowed slepton mass. This also narrows the possible mass range, because at small slepton masses, constraints from LEP and in minor extent disappearing tracks come into play. If we look for instance to the smuon case for $\Delta m = 1$ GeV, we obtain a possible mass range between 110 and 135 GeV due to the constraints of disappearing track searches. These searches constrain only a small part of the parameter space, so for an even larger mass-splitting, the lifetime can become small enough to avoid these bounds. Only then, the maximal allowed slepton mass is so low that it almost coincides with the LEP bounds. For instance, looking at the curve representing $\Delta m = 1.5$ GeV for the smuon case in figure 4.3, we obtain an allowed mass range from about 95 to 110 GeV, which is even more narrow than the range when $\Delta m = 1$ GeV. Thus, it seems that we can achieve the broadest mass range for a mass splitting around 0.5 GeV, but this does not mean that all the other possibilities are already excluded. They are just more constrained.

Conclusion

The last few decades, a considerable amount of theoretical and experimental efforts have been made to determine the nature of dark matter. Nowadays, a commonly used strategy is to make use of simplified models to describe what are the possible DM signatures in collider or other experiments. We introduced such a simplified model inspired by SUSY with a non-minimal dark sector consisting of a Majorana DM particle χ that interacts with a charged scalar $\widetilde{l}$ and a SM lepton l. There are three free parameters in this model, the DM mass m_χ, the mass-splitting between the DM and the charged scalar partner Δm and the coupling constant λ_χ.

Because we know how abundant DM is in our universe, we started by studying how the DM particle in our model could have been produced in the early universe. This is largely dependent on the free parameters of our model. Especially the coupling constant λ_χ plays an important role. We were able to define four different regimes where different production mechanisms are important:

1. The freeze-out regime with co-annihilations ($\lambda_\chi \sim 10^{-1}$),
2. The freeze-out regime driven by $\widetilde{l}\widetilde{l}^\dagger$ annihilation ($\lambda_\chi \sim 10^{-5}$),
3. The conversion-driven freeze-out regime ($\lambda_\chi \sim 5 \cdot 10^{-7}$),
4. The freeze-in regime ($\lambda_\chi \sim 10^{-8}$).

We focussed on the conversion-driven freeze-out regime as it has not yet been much studied in the literature. For this mechanism, we had to carefully threat the conversion processes $\chi \leftrightarrow \widetilde{l}$ that are suppose to happen fast in the standard freeze-out mechanism. For the latter purpose, we implemented our own code in Mathematica that included these processes such that we were able to calculate the relic abundance in every regime.

With a fully working code, we started to investigate the conversion-driven freeze-out mechanism in the context of the leptons coupling to the DM and the charged scalar. We were able to find a window of the DM mass between about 100 GeV and 200 GeV for a mass-splitting smaller than 2 GeV where the conversion-driven freeze-out reproduces the correct relic abundance. For the three cases where the

DM couples to one of the leptons, we were able to find these regions. When χ couples to τ, the interesting region where conversion-driven freeze-out reproduces the DM relic abundance is already completely excluded by searches at LEP. In the other two cases, there is still a portion of this region unconstrained by LEP. From this point onwards, we focussed only on muon and electron coupling to the DM and studied how the charged scalar can give new signatures at collider experiments compared to the traditional prompt decay searches.

If the coupling constant λ_χ is small enough, the decay length of the slepton can become macroscopic. This happens for the model under study when the conversion-driven freeze-out mechanism reproduces the correct relic abundance which makes this region interesting. If the charged scalars have a long lifetime, they are not included in the traditional prompt decay searches. We have reviewed the most important long-lived slepton searches and looked at how they constrain our model. We saw that especially the searches for heavy stable charged particles poses strong bounds on the charged scalars with a decay length of the order of a few meters. However, for smaller lifetimes, the constraints are not as stringent. The most important limits come from LEP which constrain small masses of the charged scalar ($m_{\tilde{l}} < 100$ GeV). Besides searches from LEP, also disappearing track searches sets bounds on charged leptons with a decay length of about 50 cm. If the mass-splitting between the DM and charged scalar is small enough, our model can accommodate the observed relic DM abundance for masses up to 200 GeV. This means that there is still a reasonably large phenomenological viable mass range which is unconstrained.

These results are obtained for the simplified model where we ignored the term in the Lagrangian describing possible interactions between the Higgs and the charged scalars. Our results are still valid if the coupling that governs these reactions is sufficiently small. Including the term in the Lagrangian might be a topic for future research.

The general conclusion we can make is that charged particles with a macroscopic decay length smaller than a few metres are still largely unconstrained and that there are models that can predict the correct relic abundance with a coupling small enough such that the decay length is of this order. It is therefore very interesting to investigate the displaced lepton and disappearing track signatures in collider experiments more extensively. This might lead to the dark matter signal researchers are already looking for a long time.

Appendix A

Analysis for the squarks

All the important processes that influence the abundance of χ if it couples to one of the squarks are very similar as for the slepton case. For instance, the co-annihilation and conversion processes for $\widetilde{b}$ can be found respectively in tables A.1 and A.2. The main difference with the case of the sleptons is that here, strong processes with gluons occur. These are strong interactions and that is why the rates including processes with gluons are larger than with the sleptons. These higher rates result in the fact that decoupling happens later and therefore, the final abundance is smaller. In section 3.1, we saw that if the relic abundance calculated while chemical equilibrium is assumed is below 0.12, conventional freeze-out cannot be the correct production mechanism and we get into the realm of conversion-driven freeze-out. This means that for the staus, the region parameter space where we need the conversion driven solution is larger due to the higher rates. If we compare the analysis done here for the sleptons with the literature (see [49] and [50]), we can see clearly that we can go to higher values for the mass and mass splitting and still obtain the correct abundance with the conversion-driven freeze-out mechanism.

initial state		final state		scaling
χ	χ	b	$\bar{b}$	λ_χ^4
χ	$\widetilde{b}$	b	g, γ, Z, H	λ_χ^2
		W^-	b	
$\widetilde{b}$	$\widetilde{b}^\dagger$	g, γ, Z, W^+	g, γ, Z, W^-	λ_χ^0
		q	$\bar{q}$	
		H	Z	
		e^-, μ^-, τ^-	e^+, μ^+, τ^+	
$\widetilde{b}$	$\widetilde{b}$	b	b	λ_χ^4

Table A.1: List of all included co-annihilation processes when χ couples to the sbottom $\widetilde{b}$. Also the dependence on λ_χ for each process is presented. The $\widetilde{b}\widetilde{b}^\dagger$ annihilation into $b\bar{b}$ also has contributions scaling with λ_χ^2 and λ_χ^4.

initial state		final state		scaling
χ	b	$\widetilde{b}$	g, γ, Z, H	λ_χ^2
	g, γ, Z, H		$\bar{b}$	
	W^-		$\bar{t}$	
	t		W^+	
$\widetilde{b}$		χ	b	λ_χ^2
χ	χ	$\widetilde{b}$	$\widetilde{b}^\dagger$	λ_χ^4

Table A.2: List of all included conversion processes when χ couples to the sbottom $\widetilde{b}$. Also the dependence on λ_χ for each process is presented.

Appendix B

Numerical integration of the cross sections

In order to find the thermally averaged cross sections as a function of the temperature, we need to integrate the amplitude $\mathcal{M}$ as follows,

$$\langle\sigma_{ij}v\rangle n_{i,eq}n_{j,eq} = \frac{g_i g_j}{512\pi^5}T\int\frac{|\mathcal{M}|^2}{\sqrt{s}}K_1\left(\frac{\sqrt{s}}{T}\right)ds\ dt. \tag{B.1}$$

This integration can be done quite simple by making use of numerical software. The amplitude is different for every process and also depends on the parameters of our model: m_χ, Δm and λ_χ. If we do the calculations numerically, they have to be done for every different set of parameters. This makes it hard to do scans and therefore, it is useful to do at least a part of the calculations analytically. For this, we can use Mathematica which is a software package for both numerical and analytical calculations. Two integrations need to be done, one over the Mandelstam variable t and one over s. The integration over t runs from [53]

$$t_{min} = \left[\frac{m_1^2 - m_2^2 - m_3^2 + m_4^2}{2\sqrt{s}}\right]^2 - (p_1 + p_3)^2, \tag{B.2}$$

to

$$t_{min} = \left[\frac{m_1^2 - m_2^2 - m_3^2 + m_4^2}{2\sqrt{s}}\right]^2 - (p_1 - p_3)^2, \tag{B.3}$$

where p_1 and p_3 are the momenta in the COM frame of the respectively incoming and outgoing particles. These integration limits are process dependent which ensures that the calculation has to be done for every process separately. We calculate

$$\mathcal{M}_{int} = g_i g_j\int_{t_{min}}^{t_{max}}|\mathcal{M}|^2 dt, \tag{B.4}$$

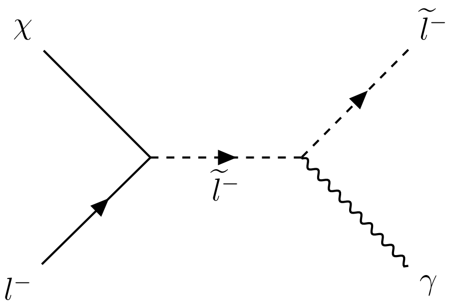

Figure B.1: Feynman diagram for the conversion process that experiences a s-channel divergence.

which includes all the process dependant information. This calculation is done analytically and the result are saved so that it only had to be done once, even if we want to do scans for different values of the parameters of the model.

Next, we have to integrate over the centre-of-mass energy s from s_{min}, which is the minimal COM energy that is needed for this process to kinematically happen, to infinity. For a general $1, 2 \to 3, 4$ process, s_{min} is the maximum of $(m_1 + m_2)^2$ and $(m_3 + m_4)^2$, where m_i is the mass of the i^{th} particle. The remaining integral reads

$$\langle \sigma_{ij} v \rangle n_{i,eq} n_{j,eq} = \frac{1}{512\pi^5} T \int_{s_{min}}^{\infty} \frac{\mathcal{M}_{int}}{\sqrt{s}} K_1 \left(\frac{\sqrt{s}}{T} \right) ds. \tag{B.5}$$

Due to the presence of the Bessel function, we can not do this integration analytically. Therefore, for every set of parameters, we define the thermally averaged cross section as a function the temperature T. This function can be obtained by calculating integral B.5 for certain values of the temperature and interpolate them to obtain a continuous function of T. To get the cross sections that are used in the Boltzmann equation, we need to group and sum the cross sections of the correct processes. How this is done can be found in appendix C.

For some processes, the calculation are not as straight forward as we mentioned here due to the presence of divergences. For instance for the process $\chi l \to \widetilde{l}\gamma$, of which the Feynman diagram can be found in figure B.1, an s-channel divergence can occur because the slepton is also the mediator for the process. In general, the amplitude squared scales like,

$$|\mathcal{M}|^2 \propto \frac{1}{s - m^2}, \tag{B.6}$$

where m is the mass of the mediator. For this process, $s_{min} = m_{\widetilde{l}}^2$ which means that the amplitude diverges at this COM energy. To solve this problem, we introduce

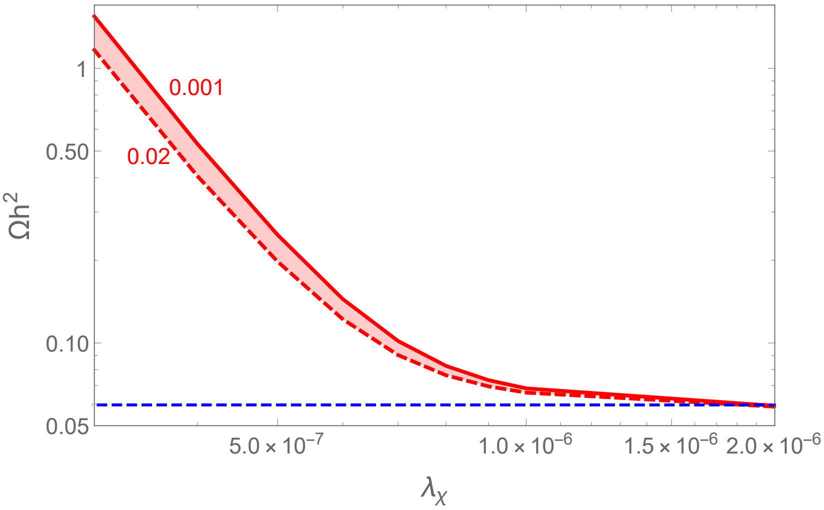

Figure B.2: Dependence of the relic DM abundance the regularization parameter $m_{cut} \in \{0.001, 0.02\} \cdot m_{\tilde{l}}$ when χ couples to $\tilde{\mu}$. The calculations are done with the parameters $m_\chi = 100$ GeV, $\Delta m = 0.5$ GeV. The blue dashed line denotes the solution when chemical equilibrium is assumed.

a cut-off such that we do start the integration at $s_{min} = (m_{\tilde{l}} + m_{cut})^2$ and we do not integrate the divergence. Of course, introducing this cut alters our results. To be certain that these changes are not large, we calculated the relic abundance for some parameters in the region we are interested and some different values for m_{cut}. The result of these calculations can be found in figure B.2. It is clear that the final DM abundance does not change dramatically, indicating that most of the interactions occur at energies well above the lepton mass. This validates the introduction of the cut on the COM energy.

A similar thing happens for the t-channel processes in figure B.3 where the mediator is the slepton with momentum p_l. The amplitude for these kind of processes scales like

$$|\mathcal{M}|^2 \propto \frac{1}{t - m^2}, \tag{B.7}$$

where $t = (p_\chi - p_{\tilde{l}})^2 = p_l^2$ and m is again the mass of the t-channel mediator. For some values of the COM energy, the lepton can go on-shell meaning that $p_l^2 = m_l^2$ and the amplitude diverges. This happens at the edge of our integration range so we can again introduce a cut such that we integrate from $t_{min} + t_{cut}$ to t_{max} and thus evade the divergence. We take as small as possible, $t_{cut} = 10^{-4} \cdot t_{min}$, such that the error we make is negligible. The dependence of this cut can be seen in figure B.4, where we plotted the relic abundance calculated for $m_\chi = 100$ GeV,

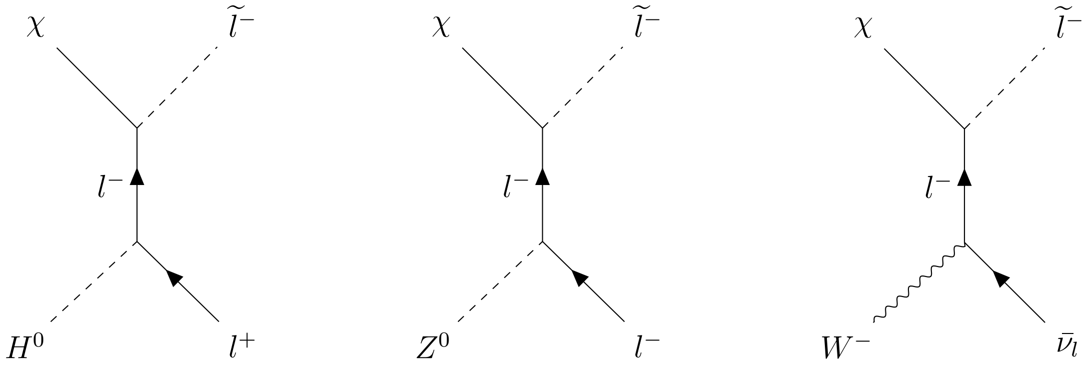

(a) (b) (c)

Figure B.3: Feynman diagrams for the conversion processes that experience a t-channel divergence.

$\Delta m = 0.5$ GeV and $\lambda_\chi = 5 \cdot 10^{-7}$ and some values of t_{cut}. There is almost no noticeable difference for small values of the cut. And even if we choose $t_{cut} = t_{min}$, the difference is less than one percent. This indicates that the processes where we introduced the cut are sub-leading and do not change the result much. Therefore, by introducing this cut, we still arrive at the same relic abundance while avoiding the divergence.

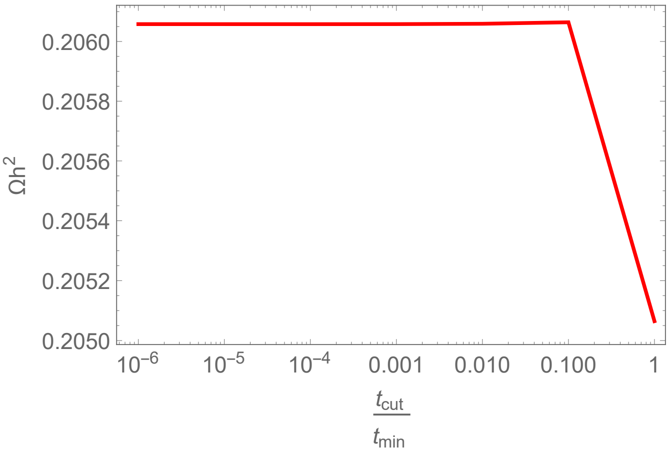

Figure B.4: Dependence of the relic abundance on the cut we made in the integration over t. The calculations are done with the parameters $m_\chi = 100$ GeV, $\Delta m = 0.5$ GeV and $\lambda_\chi = 5 \cdot 10^{-7}$.

Appendix C

Defining the rates included in the Boltzmann equation

In table 2.1 and 2.2, all the processes that influence the relic abundance are summarized. All of them have a different influence and therefore, we compare all the cross sections in section 2.3.2. More precise, we want to compare the efficiency of the processes, i.e. how they compare to the Hubble rate. If $\Gamma > H$, they are efficient and the interactions happen fast enough such that the process is in equilibrium. For $\Gamma < H$, this is not the case. To check the efficiency, we have to know how the rate Γ is defined in order to compare it to the Hubble rate. Here, we give a list of all the definitions of the rates for every process.

$$\chi\chi \to l\bar{l} : \Gamma = \frac{\langle \sigma_{\chi\chi\to l\bar{l}} v\rangle n_\chi^{eq} n_\chi^{eq}}{n_\chi^{eq}}, \tag{C.1}$$

$$\chi\widetilde{l} \to SMSM : \Gamma = \frac{\Sigma_{i,j}\langle \sigma_{\chi\widetilde{l}\to ij} v\rangle n_\chi^{eq} n_{\widetilde{l}}^{eq}}{n_{\widetilde{l}}^{eq}}, \tag{C.2}$$

$$\widetilde{\widetilde{l}\widetilde{l}}^\dagger \to SMSM : \Gamma = \frac{\Sigma_{i,j}\langle \sigma_{\widetilde{\widetilde{l}\widetilde{l}}^\dagger\to ij} v\rangle n_{\widetilde{l}}^{eq} n_{\widetilde{l}}^{eq}}{n_{\widetilde{l}}^{eq}}, \tag{C.3}$$

$$\chi SM \to \widetilde{l}SM : \Gamma = \frac{\Sigma_{i,j}\langle \sigma_{\chi i\to\widetilde{l}j} v\rangle n_\chi^{eq} n_i^{eq}}{n_\chi^{eq}}, \tag{C.4}$$

$$\widetilde{l} \to \chi l : \Gamma = \Gamma_{\widetilde{l}\to\chi b} \frac{K_1\left(m_{\widetilde{l}}/T\right)}{K_2\left(m_{\widetilde{l}}/T\right)} \frac{n_{\widetilde{l}}^{eq}}{n_\chi^{eq}}, \tag{C.5}$$

$$\chi\chi \to \widetilde{\widetilde{l}\widetilde{l}}^\dagger : \Gamma = \frac{\langle \sigma_{\chi\chi\to\widetilde{\widetilde{l}\widetilde{l}}^\dagger} v\rangle n_\chi^{eq} n_\chi^{eq}}{n_\chi^{eq}}. \tag{C.6}$$

If one compares the list above with tables 2.1 and 2.2, one can spot that there is one process missing, namely $\widetilde{\widetilde{l}\widetilde{l}} \to ll$. This process has the same influence as

$\widetilde{ll}^\dagger \to SMSM$ on the relic abundance, but it is suppressed by λ_χ^4. It is always sub-leading (unless $\lambda_\chi \approx 1$, a regime we are not interested in) and therefore, it is not include in the plots where we compare the efficiencies of the different rates or in the Boltzmann equation. If we want to go to a regime where $\lambda_\chi \approx 1$, we have to add the thermal averaged cross section of this process to the one of $\widetilde{ll}^\dagger \to SMSM$. One thing we have to consider is that in the Boltzmann equations (2.5) and (2.6), we sometimes added a factor of two to account for processes with anti-sleptons. For the $\widetilde{ll} \to ll$, we to have to add this factor too because also the process $\widetilde{l}^\dagger\widetilde{l}^\dagger \to \overline{ll}$ needs to be taken into account. This means that the Boltzmann equation for $\widetilde{l}$ reads,

$$\begin{aligned}\frac{dY_{\widetilde{l}}}{dx} = \frac{-s}{Hx}\Bigg[&\left(\langle\sigma_{\widetilde{ll}^\dagger}v\rangle + 2\langle\sigma_{\widetilde{ll}\to ll}v\rangle\right)\left(Y_{\widetilde{l}}^2 - Y_{\widetilde{l},eq}^2\right) + 2\langle\sigma_{\chi\widetilde{l}}v\rangle\left(Y_\chi Y_{\widetilde{l}} - Y_{\chi,eq}Y_{\widetilde{l},eq}\right)\\ &- \frac{2\Gamma_{\chi\to\widetilde{l}}}{s}\left(Y_\chi - Y_{\widetilde{l}}\frac{Y_{\chi,eq}}{Y_{\widetilde{l},eq}}\right) + \frac{2\Gamma_{\widetilde{l}}}{s}\left(Y_{\widetilde{l}} - Y_\chi\frac{Y_{\widetilde{l},eq}}{Y_{\chi,eq}}\right)\\ &- \langle\sigma_{\chi\chi\to\widetilde{ll}^\dagger}v\rangle\left(Y_\chi^2 - Y_{\widetilde{l}}^2\frac{Y_{\chi,eq}^2}{Y_{\widetilde{l},eq}^2}\right)\Bigg]. \qquad \text{(C.7)}\end{aligned}$$

Bibliography

[1] G. Arcadi, M. Dutra, et. al., *The Waning of the WIMP? A Review of Models, Searches, and Constraints.* (2017) arXiv:1703.07364 [hep-ph].

[2] J. L. Feng, A. Rajaraman and F. Takayama, *Superweakly Interacting Massive Particles.* (2003) arXiv:hep-ph/0302215.

[3] L. J. Hall, K. Jedamzik, J. March-Russel and S. M. West, *Freeze-In Production of FIMP Dark Matter.* (2009) arXiv:0911.1330 [hep-ph].

[4] C. Cheung, G. Elor, L. J. Hall and P. Kumar, *Origins of Hidden Sector Dark Matter I: Cosmology.* (2010) arXiv:1010.0022 [hep-ph].

[5] K. Petraki and R. R. Volkas, *Review of asymmetric dark matter.* (2013) arXiv:1305.4939 [hep-ph].

[6] D. Abercrombie, N. Akchurin, et. al., *Dark Matter Benckmark Models for Early LHC Run-2 Searches: Report of the ATLAS/CMS Dark Matter Forum.* (2015) arXiv:1507.00966 [hep-ex].

[7] F. Zwicky, *Die Rotverschiebung von extragalaktischen Nebeln.* (1933) Helvetica Physica Acta, 6, p. 110.

[8] E. Hubble and M. L. Humason, *The Velocity-Distance Relation among Extra-Galactic Nebulae.* (1931) Astrophys. J., vol. 74, p. 43.

[9] H. W. Babcock, *The Rotation of the Andromeda Nebula.* (1939) Lick Observatory Bulletin, no. 498, p. 41.

[10] K. Freese, *Review of Observational Evidence for Dark Matter in the Universe and in Upcoming Searches for Dark Stars.* (2008) arXiv:0812.4005 [astro-ph].

[11] R. Scarpa, *Modified Newtonian Dynamics, an Introductory Review.* (2006) arXiv:astro-ph/0601478.

[12] N. W. Boggess, et al., *COBE mission: Its design and performance two years after launch.* (1992) Astrophys. J., vol. 397, no. 2, P. 420-429.

[13] E. Komatsu and C. L. Bennett, *Results from the Wilkinson Microwave Anisotropy Probe.* (2014) arXiv:1404.5415 [astro-ph.CO].

[14] G. Bertone, D. Hooper, and J. Silk, *Particle Dark Matter: Evidence, Candidates and Constraints.* (2008) Arxiv:hep-ph/0404175v2.

[15] Planck Collaboration, *Planck 2015 results. XIII. Cosmological parameters.* (2015) arXiv:1502.01589v3.

[16] M. Roos, *Dark Matter: The evidence from astronomy, astrophysics and cosmology.* (2010) arXiv:1001.0316v2.

[17] R. Massey, T. Kitching and J. Richard, *The dark matter of gravitational lensing.* (2010) arXiv:1001.1739 [astro-ph.CO].

[18] G. Bertone, and D. Hooper, *A History of Dark Matter.* (2016) arXiv:1605.04909.

[19] C. Weinheimer, *The neutrino mass direct measurements.* (2003) arXiv:hep-exp/0306057

[20] C. Csaki and P. Tanedo, *Beyond the Standard Model.* (2016) arXiv:1602.04228 [hep-ph].

[21] K. Abazajian, G. M. Fuller, and M. Patel, *Sterile neutrino hot, warm and cold dark matter.* (2001) arXiv:astro-ph/0101524.

[22] K. Agashe, and S. Géraldine, *Warped Unification, Proton Stability and Dark Matter.* (2004) arXiv:hep-ph/0403143v3.

[23] R. D. Peccei, *The Strong CP Problem and Axions.* (2006) arXiv:hep-ph/0607268v1.

[24] D. J. E. Marsh, *Axions and ALP's: a very short introduction.* (2017) arXiv:1712.03018v1.

[25] S. P. Martin, *A Supersymmetry Primer.* (2016) arXiv:hep-ph/9709356v7.

[26] B. Carr, F. Kühnel, and M. Sandstad, *Primordial Black Holes as Dark Matter.* (2017) arXiv:1607.060774v4.

[27] M. Sasaki, T. Suyama, T. Tanaka and S. Yokoyama, *Primordial Black Hole Scenario for the Gravitational-Wave Event GW150914.* (2016) arXiv:1603.08338 [astro-ph.CO].

[28] X. Chu, T. Hambye and M. H. G. Tytgat, *The Four Basic Ways of Creating Dark Matter Through a Portal.* (2012) arXiv:1112.0493 [hep-ph].

[29] S. Dodelson, *Modern Cosmology* (2003) Academic Press.

[30] F. Tanedo, *Defense against the dark arts.* (2011) `www.physics.uci.edu/~tanedo/files/notes/DMNotes.pdf`

[31] Wolfram Research, Inc., Mathematica, Version 11.3, Champaign, IL (2018).

[32] J. Heeck and D. Teresi, *Cold keV dark matter from decays and scatterings.* (2017) arXiv:1706.09909 [hep-ph].

[33] L. J. Hall, K. Jedamzik, J. March-Russel, and S. W. West, *Freeze-In Production of FIMP Dark Matter.* (2009) arXiv:0911.1120v2.

[34] N. Bernal, M. Heikinheimo, T. Tenkanen, K. Tuominen, and V. Vaskonen, *The Dawn of the FIMP Dark Matter: A Review of Models and Constraints.* (2017) arXiv:1706.07442v2.

[35] K. Griest, and D. Seckel, *Three Exceptions in the Calculation of Relic Abundances.* Phys. Rev. D43 (1991) 3191-3203

[36] XENON Collaboration, *Dark Matter SEarch Results from a One Tonne × Year Exposure of XENON1T.* (2018) arXiv:1805.12562 [astro-ph.CO].

[37] LUX Collaboration, *Results from a search for dark matter in the complete LUX exposure.* (2016) 1608.07648 [astro-ph.CO].

[38] PandaX-II Collaboration, *Dark Matter Results from 54-Ton-Day Exposure of PandaX-II Experiment.* (2017) arXiv:1708.06917 [astro-ph.CO].

[39] E. Mocchiutti, O. Adriani, et al., *The PAMELA Space Experiment.* (2009) arXiv:0905.2551.

[40] Kounine, A., *AMS Experiment on the International Space Station.* (2011) `http://inspirehep.net/record/1352202/files/vc_I02.pdf`

[41] V. A. Mitsou, *Overview of searches for dark matter at the LHC.* (2015) J. Phys.: Conf. Ser. 651 012023.

[42] P. De Jong, *Supersymmetry searches at the LHC.* (2012) arXiv:1211.3887 [hep-ex].

[43] T. Plehn, *Yet Another Introduction to Dark Matter.* (2017) arXiv:1705.01987 [hep-ph].

[44] J. Abdallaha, H. Araujob, et. al., *Simplified Models for Dark Matter Searches at the LHC.* (2015) arXiv:1506.03116 [hep-ph].

[45] A. De Simone and T. Jacques, *Simplified Models vs. Effective Field Theory Approaches in Dark Matter Searches.* (2016) arXiv:1603.08002 [hep-ph].

[46] M. Duerr, F. Kahlhoefer, K. Schmidt-Hoberg, T. Schwetz and S. Vogl, *How to save the WIMP: global analysis of a dark matter model with two s-channel mediators.* (2016) arXiv:1606.07609 [hep-ph].

[47] A. Davoli, A. De Simone, T. Jacques and V. Sanz, *Displaced Vertices from Pseudo-Dirac Dark Matter.* (2017) arXiv:1706.08985 [hep-ph].

[48] E. Kh. Akhmedov, *Majorana neutrinos and other Majorana particles: Theory and experiment* (2014) arXiv:1412.3320 [hep-ph].

[49] M. Garny, J. Heisig, B. Lülf, and S. Vogl, *Co-annihilation without chemical equilibrium.* (2017) arXiv:1705.09292.

[50] M. Garny, J. Heisig, M. Hufnagel, and B. Lülf, *Top-philic dark matter within and beyond the standard WIMP paradigm.* (2018) arXiv:1802.00814.

[51] A. Alloul, N. D. Christensen, C. Degrande, C. Duhr, and B. Fuks, *FeynRules 2.0 - A complete toolbox for tree-level phenomenology.* (2013) arXiv:1308.4955.

[52] A. Belyaev, N. D. Christensen, and A. Pukhov, *CalcHEP 3.4 for collider physics within and beyond the Standard Model.* (2012) arXiv:1207.6082.

[53] Particle Data Group, *Kinematics.* (2017) web. `http://pdg.lbl.gov/2017/reviews/rpp2017-rev-kinematics.pdf`.

[54] G. Belanger, F. Boudjema, A. Pukhov and A. Semenov, *micrOMEGAs: A program for calculating the relic density in the MSSM.* (2001) arXiv:hep-ph/01122787.

[55] Particle Data Group, *Supersymmetric Particle Searches.* (2017) web. `http://pdg.lbl.gov/2017/listings/rpp2017-list-supersymmetric-part-searches.pdf`

[56] The DELPHI Collaboration, *Search for supersymmetric particles assuming R-parity non-conservation in* e^+e^- *collisions at* $\sqrt{s}$ *= 192 to 208 GeV.* (2004) arXiv:hep-ex/0406009.

[57] DELPHI Collaboration, *Searches for supersymmetric particles in* e^+e^- *collisions up to 208 GeV and interpretation of the results within the MSSM.* (2003) arXiv:hep-ex/0311019.

[58] The ALEPH Collaboration, *Absolute Lower Limits on the Masses of Selectrons and Sneutrinos in the MSSM.* (2002) arXiv:hep-ex/0207056.

[59] M. J. Baker, J. Brod, et. al., *The Coannihilation Codex.* (2015) arXiv:1510.03434 [hep-ph].

[60] A. Linde, *Inflationary Cosmology.* (2007) 0705.0164 [hep-th].

[61] S. Nurmi, T. Tenkanen and K. Tuominen, *Inflationary Imprints on Dark Matter.* (2015) arXiv:1506.04048 [astro-ph.CO].

[62] V. V. Khoze, A. D. Plascencia and K. Sakurai, *Simplified models of dark matter with a long-lived co-annihilation partner.* (2017) arXiv:1702.00750 [hep-ph].

[63] The CMS Collaboration, *Observation of a new boson at a mass of 125 GeV with the CMS experiment at the LHC.* (2012) arXiv:12077235 [hep-ex].

[64] The ATLAS Collaboration, *Observation of a New Particle in the Search for the Standard Model Higgs Boson with the ATLAS Detector at the LHC.* (2012) arXiv:1207.7214 [hep-ex].

[65] G. F. Guidice, and R. Rattazzi, *Theories with gauge mediated supersymmetry breaking.* (2016) arXiv:hep-ph/9801271.

[66] D. Barney, *CMS detector slice.* web. `http://cds.cern.ch/record/2120661/files/`.

[67] CERN, *How a detector works* (2018) web. `https://home.cern/about/how-detector-works`.

[68] The CMS Collaboration, *Search for selectrons and smuons at* $\sqrt{s} = 13\ TeV$. (2017) CMS PAS SUS-17-009.

[69] The CMS Collaboration, *Searches for long-lived charged particles in pp collisions at* $\sqrt{s} = 7$ *and 8* TeV. (2013) arXiv:1305.0491v2 [hep-ex].

[70] The OPAL Collaboration, *Searches for Gauge-Mediated Supersymmetry Breaking Topologies in e^+e^- Collisions at LEP2.* (2005) arXiv:hep-ex/0507048.

[71] The CMS Collaboration, *Search for disappearing tracks in proton-proton collisions at $\sqrt{s} = 8TeV$.* (2015) arXiv:1411.6006v2 [hep-ex].

[72] The ATLAS Collaboration, *Search for charginos nearly mass-degenerate with the lightest neutralino based on a disappearing-track signature in pp collisions at $\sqrt{s} = 8TeV$ with the ATLAS detector.* (2013) arXiv:1310.3675v1 [hep-ex].

[73] The CMS Collaboration, *Search for Displaced Supersymmetry in events with an electron and a muon with large impact parameters.* (2015) arXiv:1409.4789v2 [hep-ex].

[74] J. A. Evans, and J. Shelton, *Long-Lived Staus and Displaced Leptons at the LHC.* (2016) arXiv:1601.01326 [hep-ph].